International Journal of Hydrogen Energy 53 (2024) 114–130

Contents lists available at ScienceDirect

International Journal of Hydrogen Energy

journal homepage: www.elsevier.com/locate/he

Proposal and validation of a numerical framework for 3D-CFD in-cylinder simulations of hydrogen spark-ignition internal combustion engines

Stefano Sfriso [a,*], Fabio Berni [a], Stefano Fontanesi [a], Alessandro d'Adamo [a], Stefano Frigo [b], Marco Antonelli [b], Massimo Borghi [a]

[a] Università Degli Studi di Modena e Reggio Emilia, Italy
[b] Università di Pisa, Italy

ARTICLE INFO

Handling Editor: Dr A Bhatnagar

ABSTRACT

In the light of the recent standards proposed by the European Union in terms of CO_2 emissions for the internal combustion engines, the attention is increasingly focused on e-fuels, among which the renewable-produced hydrogen. The present paper proposes a numerical methodology for 3D-CFD in-cylinder simulations of hydrogen-fuelled internal combustion engines. The proposed framework includes in-house developed models for ignition, knock and heat transfer and it is based on the G-equation combustion model. The predictive capabilities of the methodology are validated against experimental data on a single-cylinder naturally-aspirated diesel engine converted for spark-ignited hydrogen operation. Specifically, H_2 is direct injected thanks to two injectors installed on the cylinder head. Moreover, a spark plug is added and the compression ratio is lowered. The investigated conditions cover different revving speeds (from 1500 rpm to 3000 rpm) and equivalence ratios (0.4, 0.6 and 0.8). The satisfying agreement between numerical results and experimental counterparts paves the way to future studies (e.g. on emission modelling) and engine optimization.

1. Introduction

The increasing concern about the global warming associated to the emission of greenhouse gases such as some of the combustion products is pushing the European Union to stop CO_2 emissions from the internal combustion engines. To date, 25% of the global power generation comes from internal combustion engines, which are responsible for 10% of the greenhouse gas emissions [1]. Since traditional fossil fuels have carbon dioxide as main combustion product, alternatives for power generation are being explored.

Among the top-rated currently available technologies, there are electric motor powered by batteries (or fuel cells) supplied by green energy (or green hydrogen), and internal combustion engines powered by e-fuels. All these alternatives have advantages in specific applications and economic contexts and, thus, they are all being studied and developed. In this paper, the attention is specifically focused on hydrogen-powered internal combustion engines.

In Table 1 ([2,3]), the main combustion-related properties of the hydrogen are resumed, and briefly commented in the following, to point out potential and challenges related to the use of such e-fuel in ICEs.

Hydrogen lower heating value is almost three times higher than the gasoline one [2], while the stoichiometric air to fuel ratio is more than double. This makes the specific energy (i.e., the energy per air mass unit) of the stoichiometric air-fuel mixture in an H_2 DI engine comparable to the one of traditional carbon-based fuels. Moreover, the wide H_2 flammability limits open the scenario of engine load variations via mixture quality change [5], thus with higher efficiency [6] than throttling.

Despite the high RON, the low MON makes the knock resistance of the hydrogen critical. Several authors have proposed solutions in the past to address this problem. The most common one is the adoption of water injection in order to lower the peak temperature at the end of the compression stroke [7,8], thanks to the latent heat of vaporization of the water. Other authors used cooled EGR [9] to achieve the peak temperature lowering. Xu et al. [10] investigated the use of acoustically absorbing walls for the combustion chamber to suppress knock.

In addition, H_2 is characterized by very low Minimum Ignition Energy (MIE). Although it makes such fuel particularly suitable to be spark ignited [11], it promotes pre-ignition by hot spots [12].

The low Lewis number makes the hydrogen-air mixture flame susceptible to acceleration when positively stretched [13]. This effect

* Corresponding author.
E-mail address: stefano.sfriso@unimore.it (S. Sfriso).

https://doi.org/10.1016/j.ijhydene.2023.12.027
Received 29 March 2023; Received in revised form 9 October 2023; Accepted 4 December 2023

Table 1
Hydrogen properties [2–4].

Flammability (vol %)	4 ÷ 76
Minimum Ignition Energy, MIE (λ = 1, 1 bar, 298 K)	0.02 mJ
Storage	Compressed
Storage pressure	700 bar
Density under storage conditions	39 kg/m^3
Density (1 bar, 273 K)	0.089 kg/m^3
RON (Research Octane Number)	>130
MON (Motor Octane Number)	60
Lower Heating Value	120 MJ/kg
Quenching distance (λ = 1, 1 bar, 298 K)	0.64 mm
Adiabatic flame temperature (λ = 1, 1 bar, 298 K)	2480 °C
Laminar flame speed (λ = 1, 1 bar, 298 K)	1.85 m/s
Stoichiometric air to fuel ratio	34.4

Table 2
Stock and modified engine specifications.

N° of Cylinders	1
Valves per cylinder	2
Alimentation	Naturally aspirated
Bore	87 mm
Stroke	85 mm
Displacement	505 cm^3
Compression ratio	19:1 (Diesel), 10:1 (Hydrogen)
Max Power	9 kW @ 3600 rpm (Diesel), 9.14 kW @ 3000 rpm (Hydrogen)
Max Torque	31 Nm @ 2000 rpm (Diesel), 32.7 Nm @ 2500 rpm (Hydrogen)
Combustion initiation	CI (Diesel), SI (Hydrogen)

Fig. 1. *Piston with modified bowl* [39].

promotes, along with the low wall quenching distance, the combustion efficiency, as the mixture close to the walls and in the crevices is more likely to be oxidized. However, for the same reasons, the wall heat transfer increases, leading to lower adiabatic efficiency [14]. Therefore, the high heat loss is another challenge related to H_2 ICEs, as noted by Demuynck in Ref. [15]. Stratification of the charge is the main solution that can be found in literature to overcome this problem [16]. Takagi, for example, addressed the problem proposing the PCC combustion concept [17].

The high adiabatic flame temperature of hydrogen-air combustion favours NO_x formation [18]. Since nitrogen oxides are harmful for human health [19], they represent a critical drawback of H_2 ICEs. In literature, this problem is addressed by the adoption of EGR [20] or water injection [21], both methods reducing the peak temperature, or through the optimization of the injection law [22] to obtain an optimal mixture stratification at the end of the compression.

One of the main drawbacks of the hydrogen use in ICEs is due to its low density (Table 1), not only penalizing the on-board storage but also limiting the volumetric efficiency if H_2 is not directly injected. In fact, port injection strongly reduces the mixture inflow as a consequence of the high specific volume. Thus, direct injection (DI) is often preferred but, to avoid backflow in the intake port, it has to be delayed as much as possible. This leads to difficulties in the formation of a homogeneous mixture [22] because of a reduced mixing time before ignition. In order to allow DI without penalizing the formation of an optimal mixture, the injection has to be shortened as much as possible: this is the reason why sonic/supersonic injections generated by high-pressure injectors are often found.

In the literature dealing with experimental activities, many works are focused on DI SI hydrogen engines and, specifically, on the injection timing due to the strong impact on the NO_x emissions [23–25] with, sometimes, contradictory results [26]. Additionally, there are many experimental studies on the development of high-pressure injectors [23, 27–29], which is one of the most crucial aspects of this type of engine. On the numerical side, the available research in literature is mainly devoted to accurately characterize hydrogen jets [30–34]. In fact, on the one hand, their simulation involves numerical critical factors due to the high gas velocity, requiring a high temporal and spatial resolution. On the other hand, an accurate simulation is mandatory in order to reproduce the hydrogen-air mixing process. As for the combustion process, the majority of the numerical works employs computationally expensive approaches based on detailed chemistry. For example, Liu [35] and Babayev [36] adopt the SAGE model, with the former addressing TJI H_2 combustion, and the latter compression ignition. Less expensive flamelet models are also used. Maio [37] is able to correlate CFD outcomes to experimental data using the ECFM model, but at the expense of a case-by-case calibration of the combustion model.

Moving to the present study, a DI SI engine powered by hydrogen is numerically analysed. Compared to the existing literature dealing with experiments on H_2 ICEs, the investigated engine is characterized by the use of two low-pressure injectors (6 bar). The use of two nozzles ensures a greater hydrogen flowrate, thus allowing for the recovery of the original Diesel engine power despite the low-pressure injection. This original strategy enables an easier and less expensive conversion from Diesel to hydrogen, constituting an innovative and convenient strategy. On the CFD side, the relatively low jet speed allows for a less critical simulation approach. Conversely, high-pressure injectors lead to a considerable flow velocity (with Mach numbers up to 8), necessitating the adoption of computationally expensive numerical frameworks [38]. The low-pressure injection reduces the modelling uncertainties associated with the correct representation of hydrogen jets, allowing for greater focus on the combustion modelling. This study proposes a numerical framework based on the G-equation combustion model that strongly reduces the calibration effort in 3D-CFD combustion simulations of H_2-fuelled ICEs. The model predictive capabilities are preliminarily assessed thanks to experimental data on the investigated DI SI engine, specifically in-cylinder pressure traces and combustion indicators. The effectiveness of the proposed framework encourages the adoption of the latter for future design explorations and engine calibration analyses with the aim of virtually addressing using 3D-CFD the multiple challenges related to the H_2 use in ICEs.

Following this introduction, the paper provides a description of the investigated engine and the experimental apparatus. Then, the numerical framework is described in detail and the main CFD outcomes are presented. Finally, conclusions are drawn, and the potential of the proposed modelling framework for the H_2 ICEs development is

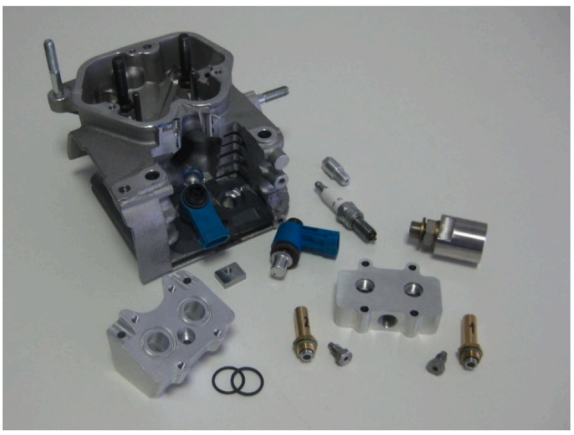

Fig. 2. *Head and additional components such as hydrogen injectors, spark plug and pressure sensor* [42].

Fig. 3. *Injector caps* [43].

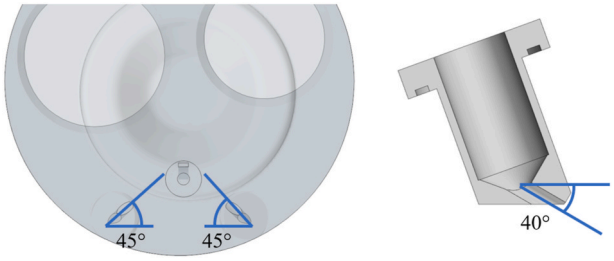

Fig. 4. Injectors cap orientation on perpendicular planes. In particular, on the left, it is possible to notice the orientation on a plane orthogonal to the cylinder axis while, on the right, the orientation with respect to the cylinder head is proposed.

discussed.

2. Experimental framework

The experimental work consists, in a first stage, in the adaptation of the original engine to hydrogen combustion [39]. Table 2 shows the specifications of the engine before and after the conversion.

The conversion to the hydrogen use is made by the adoption of two low-pressure (6 bar) injectors, a spark-plug for the ignition and the reduction of the compression ratio (CR) from 19:1 (original) to 10:1. The CR is reduced by means of both a widening of the piston bowl, which is visible in Fig. 1, and the insertion of a spacer between crankcase and cylinder. Fig. 2 shows the head components, included the additional ones used for the conversion. Preliminary analyses revealed a relevant charge stratification. For this reason, as discussed in Ref. [40], caps reported in Fig. 3 are mounted on the injector tips to guide the hydrogen jets in order to improve mixture homogeneity. The orientation of the caps adopted in this analysis to favour the charge homogeneity is proposed in Fig. 4, where the orientation on different planes is reported. Further details can be found in Ref. [41].

As shown in Table 3, a matrix of cases is tested at the bench for different speeds, namely 1500-2000-2500-3000 rpm, and equivalence ratios, namely 0.4, 0.6 and 0.8 (which in turn lead to different loads). It is interesting to remark that in Test N° 1, characterized by $\varphi = 0.8$ and 3000 rpm, the same maximum power as the original Diesel engine is achieved.

The most relevant quantities are monitored at the test bench, such as temperatures, pressures, and mass flow rates. Thermocouples monitor temperature of intake air, exhaust gases and injected H_2. Sensors are

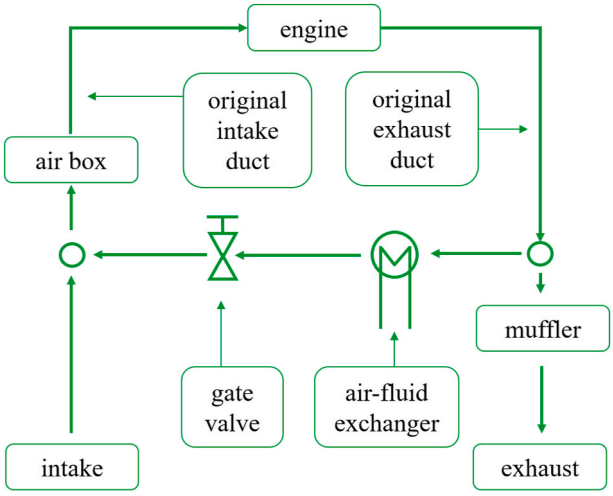

Fig. 5. Test bench scheme.

Table 3
Operating points and measured data.

Test N°	φ	SOI [° CA bTDC]	Ignition [° CA bTDC]	p H_2 [bar]	T H_2 [°C]	H_2 MFR [g/s]	Speed [RPM]	Power [kW]
1	0.80	210	−4.5	5.81	17.2	0.24663	2995	9.14
2	0.80	210	−4.5	5.83	17.5	0.21957	2501	8.55
3	0.80	220	−9	5.86	19.1	0.17173	2008	6.52
4	0.80	220	−9	5.87	19.5	0.13253	1549	4.98
5	0.60	200	3	5.85	20.2	0.18223	2995	6.15
6	0.60	200	3	5.86	20.6	0.16007	2507	6.04
7	0.60	200	3	5.89	20.7	0.12343	2011	4.62
8	0.40	200	12	5.88	21	0.12600	3003	3.28
9	0.40	200	12	5.89	21.1	0.10967	2505	3.82
10	0.40	200	12	5.91	21.3	0.08727	2015	2.94
11	0.40	200	12	5.92	21.3	0.06230	1505	1.97

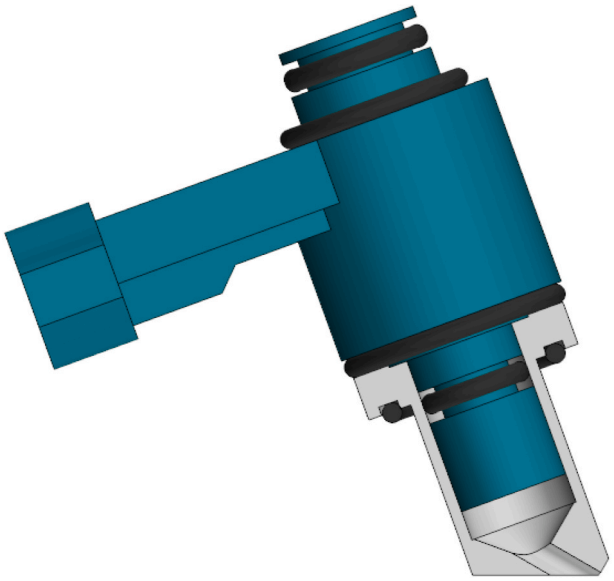

Fig. 6. Injector and cap assembly.

adopted to track the pressure of the injected H_2 and inside the cylinder.

Apparent heat release rate curves for both simulations and experiments are computed by Eq. (1) (based on the first thermodynamic law) starting from the in-cylinder pressure traces. By integrating Eq. (1), MFB profiles and, hence, combustion indicators, are obtained.

$$\frac{\delta Q}{dt} = \frac{1}{\gamma - 1} \cdot V \cdot \frac{dP}{dt} + \frac{\gamma}{\gamma - 1} \cdot P \cdot \frac{dV}{dt} \tag{1}$$

γ is the specific heat ratio of the mixture (considered as pure air for simplicity and identically treated for both simulations and testing for consistency), P is pressure and V is volume.

The air/fuel mixture quality is verified via a lambda sensor in the exhaust line. In this regard, lambda sensors are sensitive to the use of hydrogen as fuel. Therefore, during the experiments, three sensors are alternated to limit the uncertainty of the measure within a ±5 %. The accuracy is verified against data of mass flow rates for intake air and hydrogen. A schematic representation of the test bench is reported in Fig. 5. For completeness, it should be noted that the EGR line is not used in the experiments considered for the present analysis.

3. Preliminary vessel simulations

In-cylinder simulations include part of the internal portion of the H_2 injector, characterized by an annular orifice. This implies a high-resolution grid (with a characteristic cell size in the order of 10 μm, as in Ref. [38]) needed to discretize the internal nozzle annular channel. In order to limit the CFL number (which is already critical considering that the H_2 flow is sonic), small volume cells lead in turn to reduced time-step values, with a further increase of the computational cost. In addition, since H_2 injection occurs in the small volume between nozzle and cap as visible in Fig. 6, such volume should be meshed as well. Therefore, preliminary vessel simulations are carried out to evaluate the possibility to simplify the computational domain in proximity of the injector. The elimination of both the inner portion of the injector and of the cap volume prevents the use of very small cells and time-steps. The adopted numerical setup for the vessel simulations is presented at first, then results are shown.

3.1. Numerical setup

3D-CFD vessel simulations consist in test cases characterized by a simplified geometry compared to the cylinder one, in order to facilitate and speed-up the analysis. In particular, the combustion chamber volume is included in the simplified form of a fixed flat-piston cylinder (with mass exchange possible only via the H_2 inlet) with no valves. Moreover, the geometrical symmetry is exploited, thus only one of the two injectors is included and half of the cylinder is considered. Simplifications on the chamber are allowed as the attention is focused on the injector. Two configurations are tested and visible in Fig. 7: the first one (A) with the complete injector geometry and the second one (B) including only the cap hole.

Fig. 8 shows the section downstream of the inlet which is considered to monitor the average temperature and the hydrogen mass flow rate. The same section is used for both the simplified version and the full-geometry one, as it can be noticed comparing Fig. 8A) and B).

Simulations are performed using SIMCENTER STAR-CCM+, licensed by SIEMENS. The Realizable k-ε turbulence model is used, with a low-Reynolds approach, despite the in-cylinder simulations are carried out by the k-ε RNG model (as it will described in the following). The reason is that the low-Reynolds version of the RNG model is not available in STAR-CCM+, thus the most similar model is adopted. Moreover, in a previous study conducted by Pavlovich [44], it was observed that when simulating supersonic jets in open vessels, also the Realizable k-ε

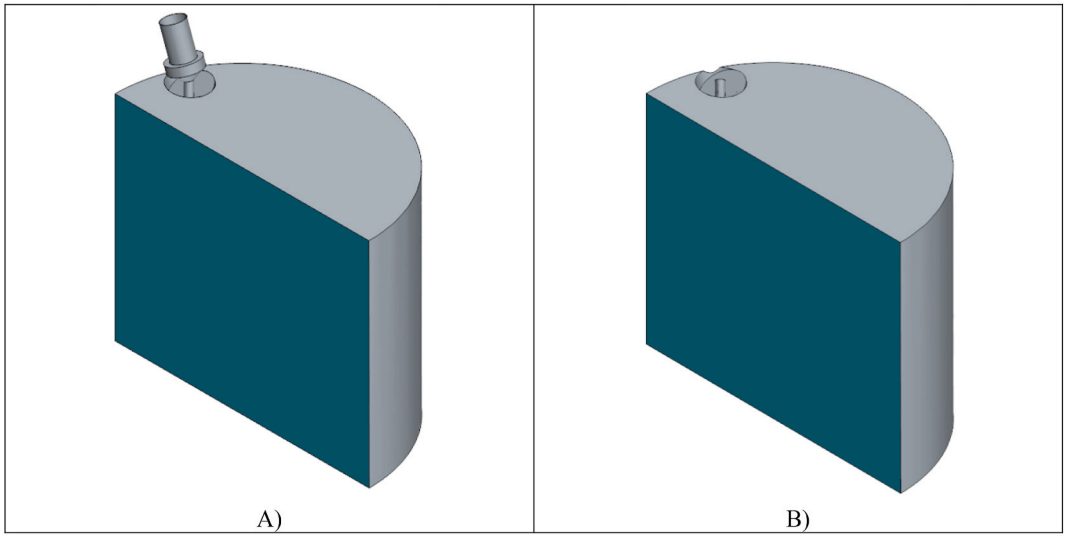

Fig. 7. Vessel geometries A) and B) are shown on the left and on the right, respectively.

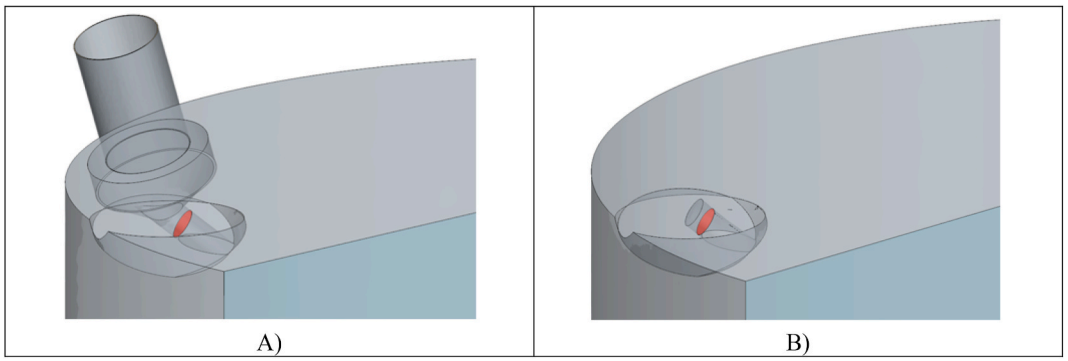

Fig. 8. Monitoring sections on geometry A) (on the left) and B) (on the right).

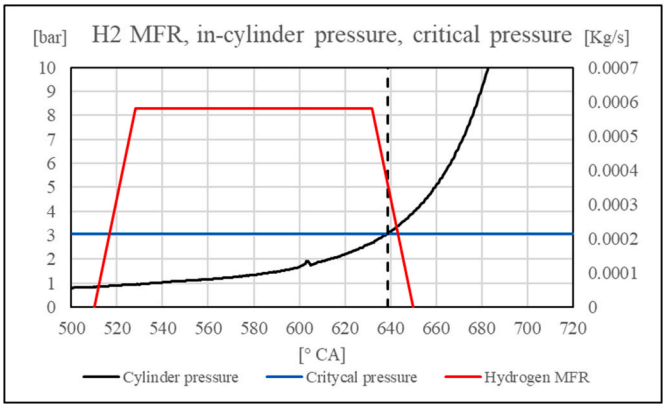

Fig. 9. Critical pressure, experimental in-cylinder pressure and hydrogen mass flow rate for case 1 of Table 3.

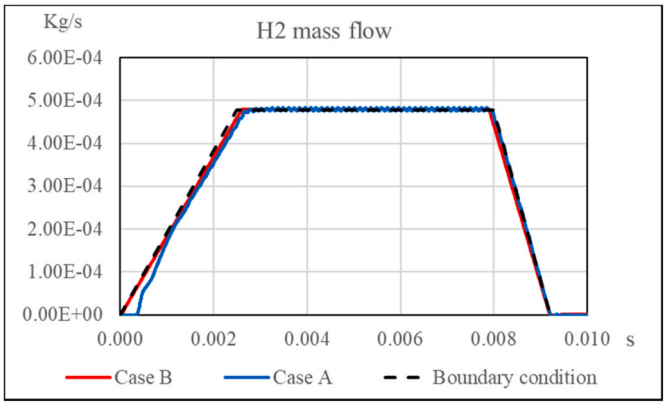

Fig. 10. Imposed (dotted line) and computed (solid lines) mass flow rates.

turbulence model is able to effectively capture the flow characteristics. Finally, it is important to note that the comparison proposed in this paragraph only deals with two computational cases. In other words, it is a purely numerical analysis and no comparison against experiments is considered.

In the light of the sonic/supersonic velocity and the Joule-Thomson effect, the fluid is simulated as a real gas, via the Soave-Riedlich-Kwong model.

At the hydrogen inlet boundary, an experimentally derived trapezoidal injection law is imposed for the mass flow rate, while the H_2 total temperature is 293 K. The same mass flow rate and total temperature are applied to both the configurations.

In order to select the initial vessel pressure, the actual injection

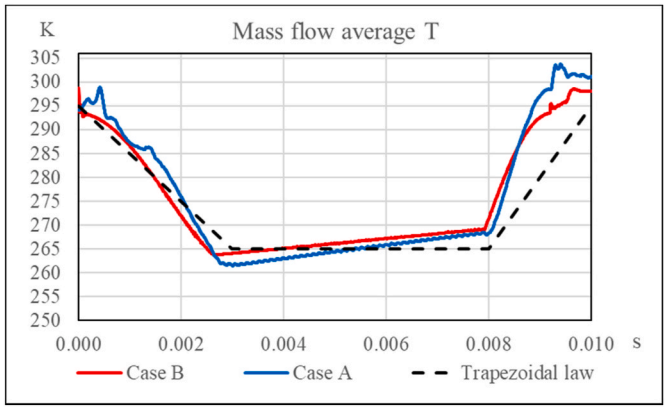

Fig. 11. Computed (solid lines) and extrapolated (dotted line) static temperature traces.

process occurring in the engine is investigated to verify the presence of a choked flow for the whole injection duration of each condition. For the purpose, the first operating condition of Table 3 is considered as it is the most critical one, having the greatest injected mass and the lowest available time before combustion (because of the highest revving speed). As a result, the injection terminates in proximity of the TDC, with a high in-cylinder back-pressure.

In order to confirm the choked flow, the critical static pressure below which a sonic flow verifies is calculated as in Eq. (2), using the throat section and the injector inlet pressure and temperature, p_{inlet} as the inlet total pressure and k as the ratio of the specific heats.

$$p_{crit} = p_{inlet}\left(\frac{2}{k+1}\right)^{\frac{k}{k-1}} \tag{2}$$

Fig. 9 shows the H_2 mass flow rate, the critical pressure and the experimental in-cylinder pressure for case 1 of Table 3. The black dashed curve points out the CA at which the in-cylinder pressure equals the critical one. Therefore, comparing the injection law and the dashed line, almost the entire injection (apart from the very last CAs) takes place at sonic conditions, terminating immediately after that chamber pressure rises above p_{crit}. This is even more true for the other conditions in which, as previously anticipated, injection terminates earlier.

Since the injector always operates with choked flow, the injection flow is independent of the downstream condition. Therefore, the chamber pressure to be adopted in the preliminary vessel simulations discussed in the present paragraph is set to an arbitrary constant value (equal to 2 barA) below the critical pressure. Wall temperatures are set to 300 K, the adopted timestep is 5×10^{-6} s and the characteristic mesh size is 0.5 mm. Localized mesh refinements of 0.2 mm are introduced around the injector in both the tested configurations.

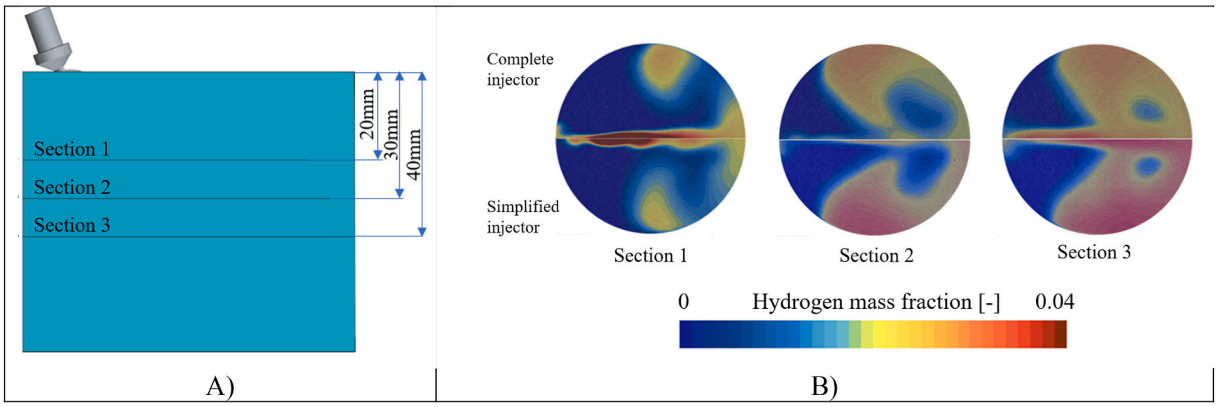

Fig. 12. Monitoring sections and corresponding comparisons between complete and simplified cases.

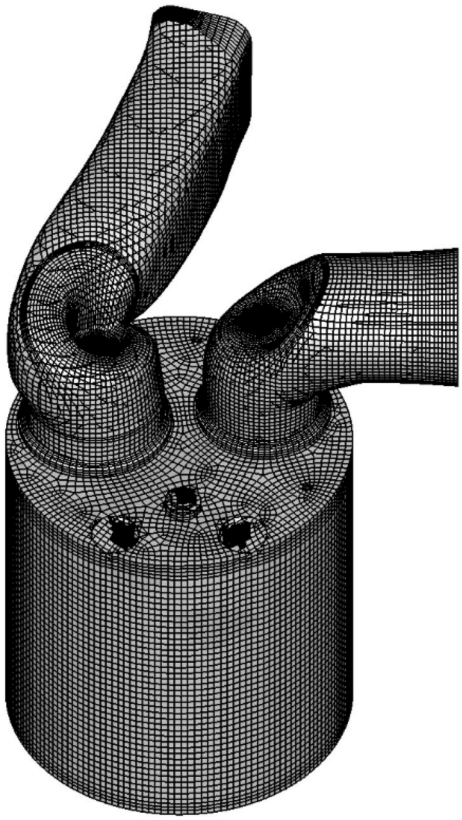

Fig. 13. Computational mesh at BDC.

3.2. Results

Fig. 10 shows the trapezoidal mass flow rate (dotted line) imposed at the inlet boundary of both the tested configurations and it is almost perfectly superimposed to the hydrogen mass flow (red line) recorded at the monitoring boundary of case B. The mass flow rate for the case A shows a little delay in the early phase due to the time needed to fill the fluid volume between injector and cap. Since such delay is almost irrelevant, the impact of the of injector simplification is considered as negligible.

The total temperature is almost entirely conserved from the original to the simplified inlet boundary, since the heat losses in the region eliminated from the configuration B are negligible. Therefore, the static temperature on the monitored section is very close between case A and B. This result further justifies the geometrical simplification. Since the software used for the in-cylinder simulations needs the hydrogen static temperature at the inlet (instead of the total one), a trapezoidal law is derived from the results of Fig. 11 and it is the dashed line reported in the same figure. This is adopted in the in-cylinder simulations described in the next paragraph.

As a further confirmation that it is possible to simplify the injector geometry without penalizing the quality of the results, the fuel concentration distribution is reported in Fig. 12 during the injection process for both the original geometry and the simplified one. The distribution is similar between the two configurations.

4. IN-CYLINDER simulations

Moving to the in-cylinder simulations, the numerical setup is extensively described at first, then results are proposed and compared to the experimental counterpart, in order to validate the proposed numerical framework.

4.1. Numerical setup

Once the geometry is defined (balancing computational cost and accuracy), attention can be focused on in-cylinder simulations. Numerical and physical setup are reported hereafter.

A RANS approach to turbulence is employed. Specifically, the k-ε RNG model [45,46] is preferred, as proficiently utilized in literature and by authors in previous analyses [47–52]. A high-Reynolds wall treatment is chosen in conjunction with a 0.3 mm thick prismatic layer on all the solid surfaces. Since a high-Reynolds approach is employed, the Improved GruMo-UniMORE heat transfer model developed by the authors [53–55] is adopted, accounting for the actual mixture Prandtl number and able to predict near wall quantities independently from near-wall grid resolution.

The core mesh size is fixed at 2 mm with local refinement regions (at the spark plug and in correspondence of the simplified injectors) characterized by a size of 1.0 mm. This setup leads to a maximum number of cells (at BDC) equal to 320 k. In this regard, a mesh sensitivity analysis, reported in Appendix A, is carried out to prove that further refinements of the grid are not able to sensibly impact the results. The adopted computational mesh is reported in Fig. 13.

The time step is chosen equal to 0.05° CA (corresponding to 2.77×10^{-6} s at 3000 rpm, 3.33×10^{-6} s at 2500 rpm, 4.16×10^{-6} s at 2000 rpm and 5.55×10^{-6} s at 1500 rpm) during valves opening and closing, injection and combustion, while 0.1° CA (corresponding to 5.54×10^{-6} s at 3000 rpm, 6.66×10^{-6} s at 2500 rpm, 8.32×10^{-6} s at 2000 rpm and 1.11×10^{-6} s at 1500 rpm) is adopted in the rest of the cycle.

Constant values are adopted for pressure and temperature on intake and exhaust boundaries, with temperature values available from the experiments. The exhaust pressure is set equal to the atmospheric one.

Table 4
Wall temperatures.

Combustion dome	523 K
Piston crown	523 K
Cylinder wall	453 K
Intake valve stem and port	320 K
Intake valve face	420 K
Exhaust valve stem	720 K
Exhaust valve face	720 K
Exhaust port	473 K
Spark plug	600 K

Table 5
Equivalence ratio, pressure and temperature at ST.

Revving Speed [rpm]	ER	P [bar]	T [K]
1500	0.4	16.0	765
	0.8	23.6	806
2000	0.4	16.6	762
	0.6	21.7	813
	0.8	24.3	807
2500	0.4	17.0	764
	0.6	22.8	814
	0.8	26.3	819
3000	0.4	16.2	768
	0.6	22.2	820
	0.8	24.5	821

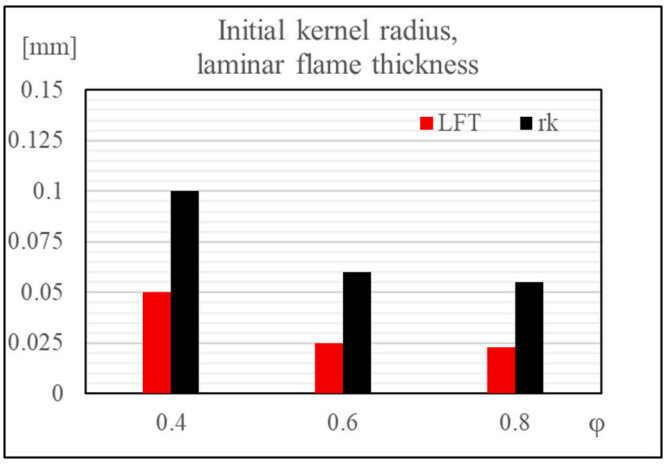

Fig. 14. Laminar Flame Thickness (LFT) and initial radius values for the operating conditions at 2000 rpm.

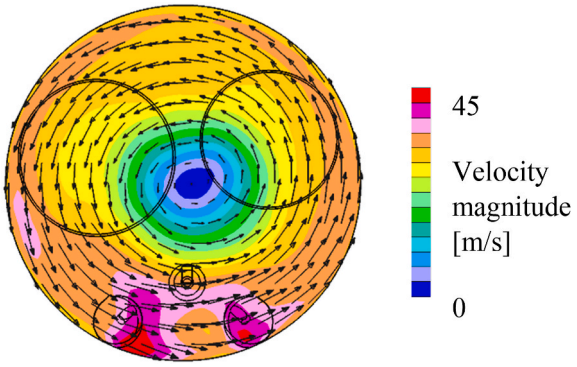

Fig. 15. Velocity field at 700° CA.

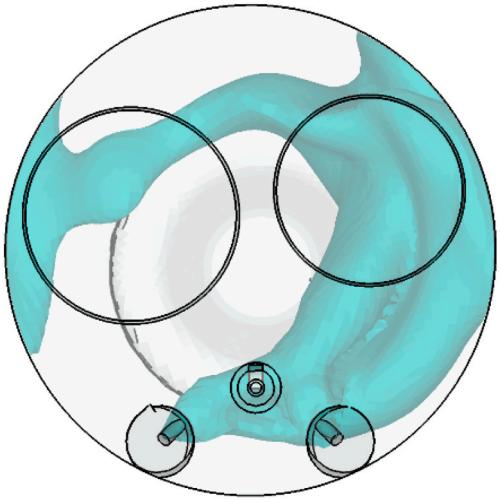

Fig. 16. The iso-surface at $\varphi = 1$ shows the impact of the swirl motion on the distribution of the hydrogen plumes for the case at $\varphi = 0.8$ and 3000 rpm.

The intake pressure is calibrated to match the experimentally-derived cycle-averaged trapped air mass. The mass flow rate condition imposed at the H_2 inlet boundary is the same trapezoidal law adopted in the previous paragraph.

Wall temperatures are imposed following previous experiences of the authors on heat transfer analyses on both spark ignition and compression ignition engines [56–58], and the adopted values are reported in Table 4.

In order to start the combustion process (i.e., imposing an initial flame kernel and governing its growth rate), an in-house developed spark-ignition model is adopted. This model is implemented in a RANS framework and it includes many of the advancements in ignition modelling already validated for LES [59–61].

In order to simplify the modelling of the ignition process, different assumptions are made on the electrical circuit and kernel growth modelling, and briefly resumed in the following along with description of the ignition model.

The electrical circuit dynamics is not considered for two reasons. Firstly, the electrical circuit transient phase has a minor impact on the arc discharge. As reported in Refs. [62–64], the time interval between nominal spark time and break-down is equal to few microseconds (in the order of 10μs), thus negligible in terms of CA at the currently analysed revving speeds. The break-down phase is even faster, thus negligible as well. Secondly, despite the electric circuit modelling allows to check the conditions for the ignition occurrence (in terms of break-down voltage and ignition energy), this is not necessary in the present analysis, thanks to the adopted ignition system which is inherited from SI gasoline engines. In fact, nor break-down voltage neither Minimum Ignition Energy (MIE) worsen moving from traditional fuels to hydrogen, even when the latter is exploited at very lean conditions ($\varphi = 0.4$). Starting from the break-down event, Tambasco [65] shows that the addition of methane to air does not remarkably affect the break-down voltage of the latter. Moreover, in Refs. [66–68] it is shown that the break-down voltage required by the hydrogen is lower than the air one. Hence, the break-down event should not be compromised in the present analysis. Focusing on the MIE, in Ref. [69] it is shown that the value in case of hydrogen-air mixture is lower or comparable to that of traditional fuels, even in case of very lean mixtures such as those ($\varphi = 0.4$) investigated in the present study.

As for kernel formation and growth after the spark event, the numerical representation is inspired to the well diffused Herweg and Maly model [70], even if with some simplifications. From Ref. [70], Eq. (3) that governs kernel growth is inherited, where r_k is the kernel radius, ρ_u density of unburned gases, ρ_k and T_k mean density and temperature of

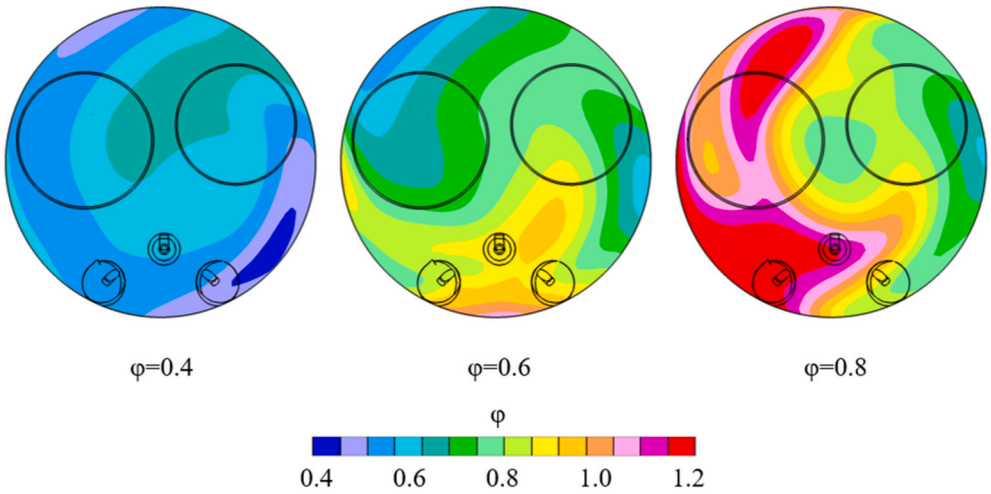

Fig. 17. Equivalence ratio at 700° CA for the 3000 rpm case.

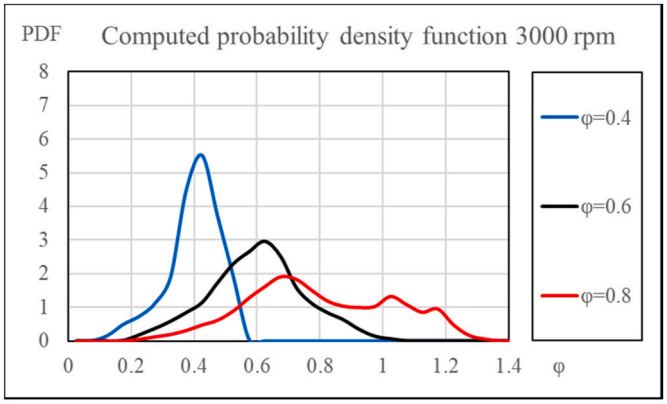

Fig. 18. Probability density function of φ for all the equivalence ratios at 3000 rpm.

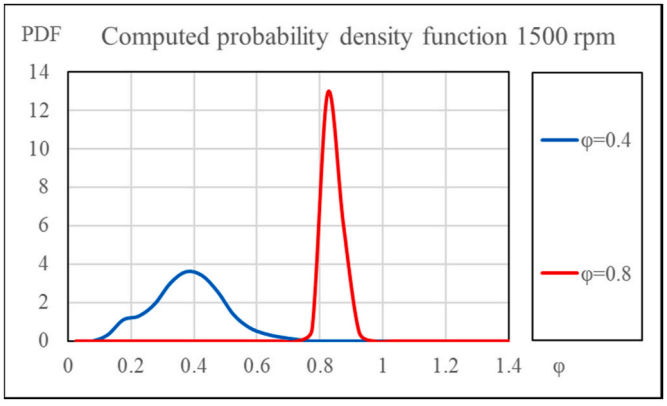

Fig. 19. Probability density function of φ for all the equivalence ratios at 1500 rpm.

the kernel. V_k and A_k are the kernel volume and surface. S_l and S_{Plasma} are laminar flame speed and expansion velocity of the plasma channel. However, compared to the original version, pressure term contribution in Eq. (3) is neglected. Moreover, the turbulent flame speed (S_T) is replaced by the laminar one (S_l). In Ref. [70], a complex expression for the turbulent flame speed is considered: in order to account for that, at very small diameters, S_T has to reduce to S_l (since the turbulence is not able to affect the kernel), while at greater values of r_k the impact of the turbulence becomes no more negligible.

$$\frac{dr_k}{dt} = \frac{\rho_u}{\rho_k}(S_l + S_{Plasma}) + \frac{V_k}{A_k}\left[\frac{1}{T_k}\frac{dT_k}{dt}\right] \tag{3}$$

In this case only S_l is considered and the turbulence contribution is neglected. This approximation is justified considering that Eq. (3) is exploited as long as kernel radius achieves 2 mm (after that, ignition model is switched off and only the G-Equation model acts governing the burn rate). As reported in Ref. [70], the contribution of the turbulence is significant just beyond radius values in the order of 2 mm.

As for S_{Plasma}, it is evaluated solving the one-dimensional unsteady heat conduction equation reported in Eq. (4), similarly to the Herweg and Maly model.

$$\rho c_p \frac{\partial T}{\partial t} = \frac{\partial}{\partial x}\left(k\frac{\partial T}{\partial x}\right) + S \tag{4}$$

ρ and c_p are density and specific heat, respectively. T and t are temperature and time. x is the space coordinate while k and S are thermal conductivity and source term. As for the plasma properties, in the present study the product ρc_p is fixed to 8000 J/(m^{3}K) and the thermal conductivity to 0.2 W/(mK). Compared to Ref. [70], S is neglected, i.e. the power provided by the ignition system is not accounted for. Using as boundary condition ($x = 0$) a temperature of $60{\cdot}10^3$ K [70], Eq. (4) limits to investigate the velocity of temperature diffusion along a specific direction starting from a high-temperature source (corresponding to the plasma channel). It is useful to point out that the initial temperature at $x = 0$ is $60{\cdot}10^3$ K, while it is equal to the unburnt temperature at $x > 0$.

Since Eq. (3) governs the kernel growth rate, an initial value for r_k is needed and it is adopted equal to $1{\cdot}10^{-4}$ m. Even if not reported here for brevity, a sensitivity on the initial r_k value is done and results do not remarkably change if lower or higher values are adopted, provided that the order of magnitude remains the same as the one of the adopted value (i.e., 10^{-4} m). Such an order of magnitude derives from an estimation of the initial burnt mass volume carried out based on the approach proposed in Ref. [71]. In particular, the initial volume of burnt mass ($V_{k,init}$) is calculated as in Eq. (5), where a cylinder of height equal to the spark gap (d_{gap}, equal to 0.5 mm in the present engine) and a radius equal to the flame thickness (δ_L) is considered. The initial radius ($r_{k,init}$) of the spherical kernel is obtain from Eq. (6).

$$V_{k,init} = d_{gap}\pi\delta_L{}^2 \tag{5}$$

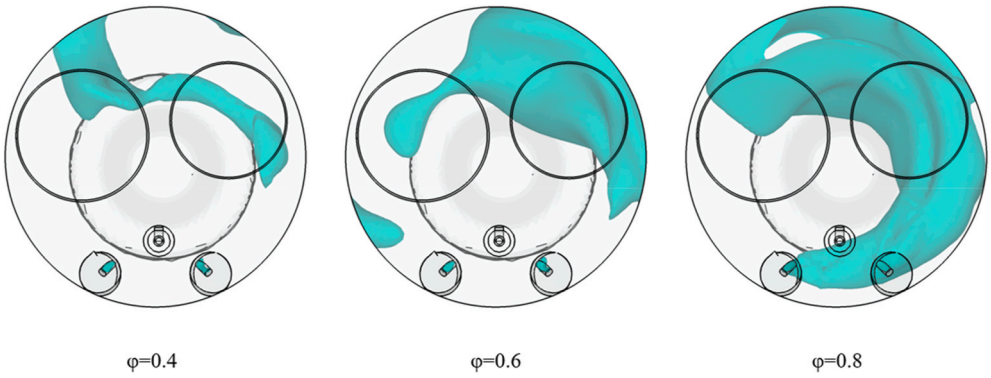

Fig. 20. φ = 1 iso-surface at the EOI for all the equivalence ratios at 3000 rpm.

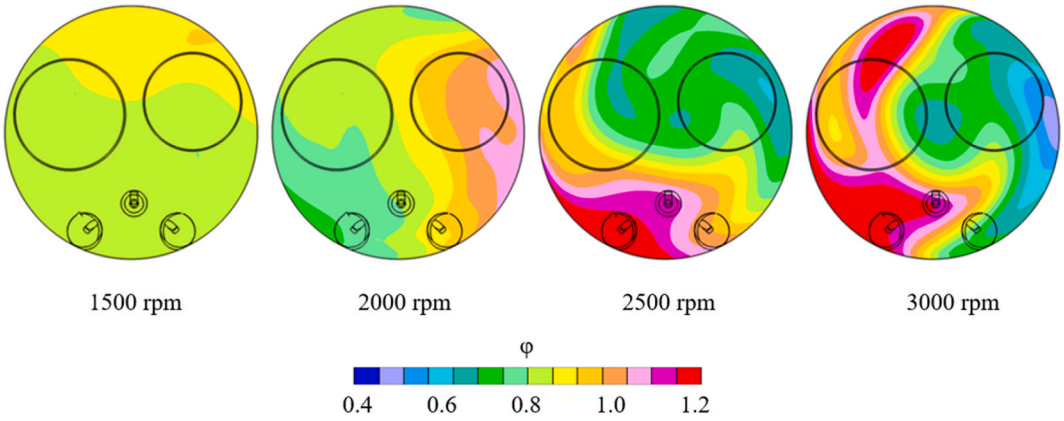

Fig. 21. Equivalence ratio at 700° CA.

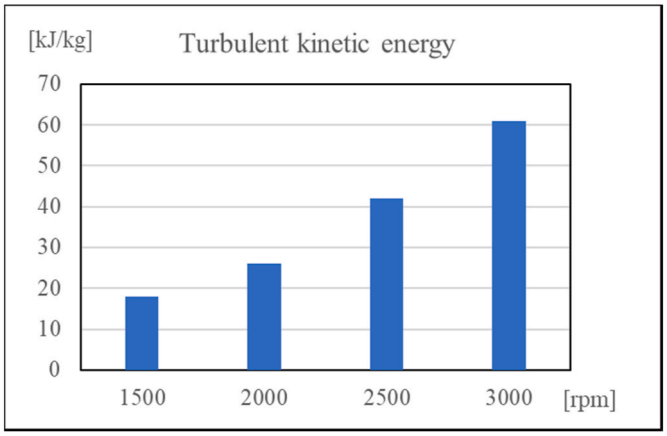

Fig. 22. Mean specific turbulent kinetic energy for the φ = 0.8 cases at 700° CA.

$$r_{k,init} = \left(\frac{3}{4\pi}V_{k,init}\right)^{1/3} \quad (6)$$

δ_L values are calculated in the present work, for the investigated operating conditions, via 1D (steady-state) freely propagating flame simulations in DARS v2020.1 licensed by SIEMENS PLM. A freely propagating flame model is a hypothetical model of a flat and infinitely large flame front propagating through a premixed medium [72]. The Shrestha [73] chemical mechanisms is adopted in this study, and simulations are carried out for all the operating conditions: pressure, temperature and equivalence ratio values for the calculations are inherited from 3D simulations and experimental data. Adopted pressure and temperature are calculated as mass-weighted averages over the computational cells constituting the combustion chamber at spark time, reported in Table 5. The equivalence ratio values are the nominal ones reported in Table 3. EGR is neglected since the concentration is minimal.

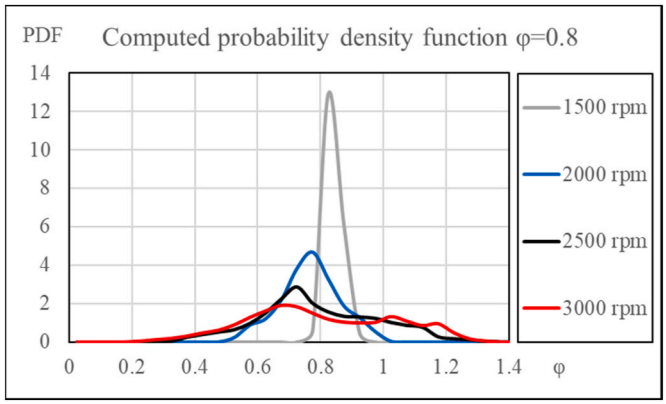

Fig. 23. Probability density function of φ for all the engine speeds at φ = 0.8.

Firstly, chemical kinetics calculations are carried out only for the operating conditions at 2000 rpm, as Table 5 shows that p and T are strongly similar for the different revving speeds, on equal equivalence ratio. Therefore, the laminar flame thickness and the initial kernel radius would be similar as well. The calculated LFT values are reported in Fig. 14 along with the resulting initial kernel radii. The latter are almost

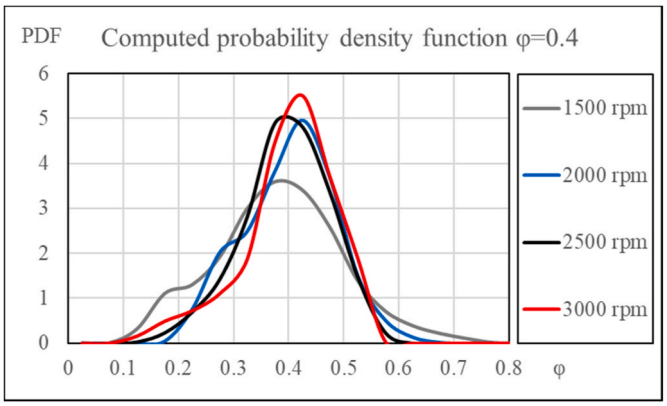

Fig. 24. Probability density function of φ for all the engine speeds in φ = 0.4 case.

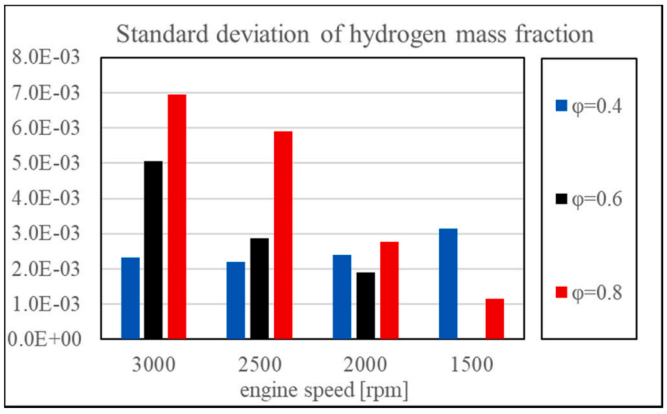

Fig. 25. Standard deviation of hydrogen mass fraction at 700° CA.

the same for the different equivalence ratios and justify the order of magnitude adopted in the present ignition model.

Combustion is modelled by G-equation, a level-set-method based combustion model which separates the burnt region from the unburnt one by an iso-surface of a scalar named G. This iso-surface is defined as the G = 0 surface. It can be seen that the G = 0 iso-surface only defines the flame front position. To describe the flame structure in turbulent flows, the variance of G is also required, from which we can obtain the turbulent flame thickness. Transport equation for G is reported in Eq. (7).

$$\frac{\partial}{\partial t}\rho G + \frac{\partial}{\partial x_i}\rho u G = \rho S_T |\nabla G| \tag{7}$$

In order to account for flame quenching at the walls, a dedicated model is adopted [74]. It is based on the calculation of a quenching distance l_q, as in Eq. (8). When the distance between a cell centroid and a wall is less than l_q, the turbulent flame speed of the cell is set to the laminar flame speed.

$$l_q = f_q\left[11.5\mu_l \Big/ \left(\rho C_\mu^{0.25} k^{0.5}\right)\right] \tag{8}$$

f_q is a parameter whose value is set to 5, as in Ref. [74]. ρ and μ_l are density and molecular viscosity, k is the turbulent kinetic energy and C_μ is the empirical coefficient adopted in the formulation of the turbulent viscosity. 11.5 represents the value of the dimensionless distance (y^+) which should act as separation point between viscous sub-layer and log-region in the boundary layer. De facto, the model establishes that below a y^+ of 57.5 (i.e. in both viscous sub-layer and buffer region) the flame stretch due to turbulence is negligible. This represents a simplification of the Bruneaux [75] model. In fact, the latter provides for a correction of the integral length scale (to be adopted in the stretch effect calculation) approaching the wall, namely for $y^+ < 50$, since vortices larger than their distance to the wall are not expected to survive. In the present model, instead, for $y^+ < 57.5$, turbulence effect on the flame speed is totally neglected.

Despite separation of burnt and unburnt gases is ideally governed by G iso-surface, the presence of a flame brush is considered by means of the definition of a reaction progress variable (c), determined by G via the algebraic relation reported in Eq. (9).

$$c = a_3\left[\mathrm{erf}\left(\frac{a_1 G}{l_{F,t}} - a_2\right) + 1\right] \tag{9}$$

$l_{F,t}$ is the turbulent flame brush thickness given by Eq. (10).

$$l_{F,t} = \alpha\frac{\sqrt{G'}}{|\nabla G|} \tag{10}$$

a_1, a_2, a_3 and α values are equal to 1.8, 0.9, 0.5 and 1, inherited from Ref. [74]. Value of c ranges from 1 (unburnt mixture) to 0 (fully burnt mixture).

The mean mass fraction of species *i* can be obtained by Eq. 11

$$Y_i = cY_{i,b} + (1-c)Y_{i,u} \tag{11}$$

where $Y_{i,b}$ is the mass fraction of species *i* in the burnt region and $Y_{i,u}$ the mass fraction of species *i* in the unburnt region. For the calculation of the burnt gas composition, the one-step reaction mechanism reported in Eq. (12) is exploited.

$$C_nH_m + \left(n + \frac{m}{4}\right)O_2 \rightarrow nCO_2 + \left(\frac{m}{2}\right)H_2O \tag{12}$$

Laminar and turbulent flame speeds are computed respectively trough Verhelst [76] and Damkholer correlations, hereafter briefly resumed. The first is based on 1D chemical kinetics computations based on the Konnov scheme [77] suitable for hydrogen oxidation, thus it does not take into account the flame instability effects associated to lean hydrogen operations. The LFS correlation is valid for p, T, φ and EGR ranges equal to 5 bar ≤ p ≤ 45 bar, 500 K ≤ T ≤ 900 K, 0.2≤φ ≤ 3, 0 mol %≤EGR≤50 mol%.

As for the turbulent flame speed, the formulation is reported in Eq. (13).

$$S_T = S_L\left(1 + A\cdot\left(\frac{u'}{S_L}\right)^{\frac{5}{6}}\right) \tag{13}$$

S_L is the laminar flame speed, u' is the root-mean-square of the turbulent velocity fluctuations. A is an empirical coefficient which is set equal to 3.3.

4.2. Results

In order to eliminate the influence of the initial conditions, multiple cycles are run for each investigated condition. For brevity, only the results of the last cycles are proposed in the following. The investigated operating points are characterized by the set of equivalence ratio and revving speed values presented in Table 3. This allows to validate the simulation framework capabilities on a wide range of conditions (in terms of turbulence and mixture quality).

4.2.1. Cold flow

Before considering the hot portion of the cycle, attention is focused on the mixture preparation. The latter is strongly influenced by the flow field. The swirling motion inherited from the original Diesel operation and due to the intake port shape is clearly visible in Fig. 15, where the

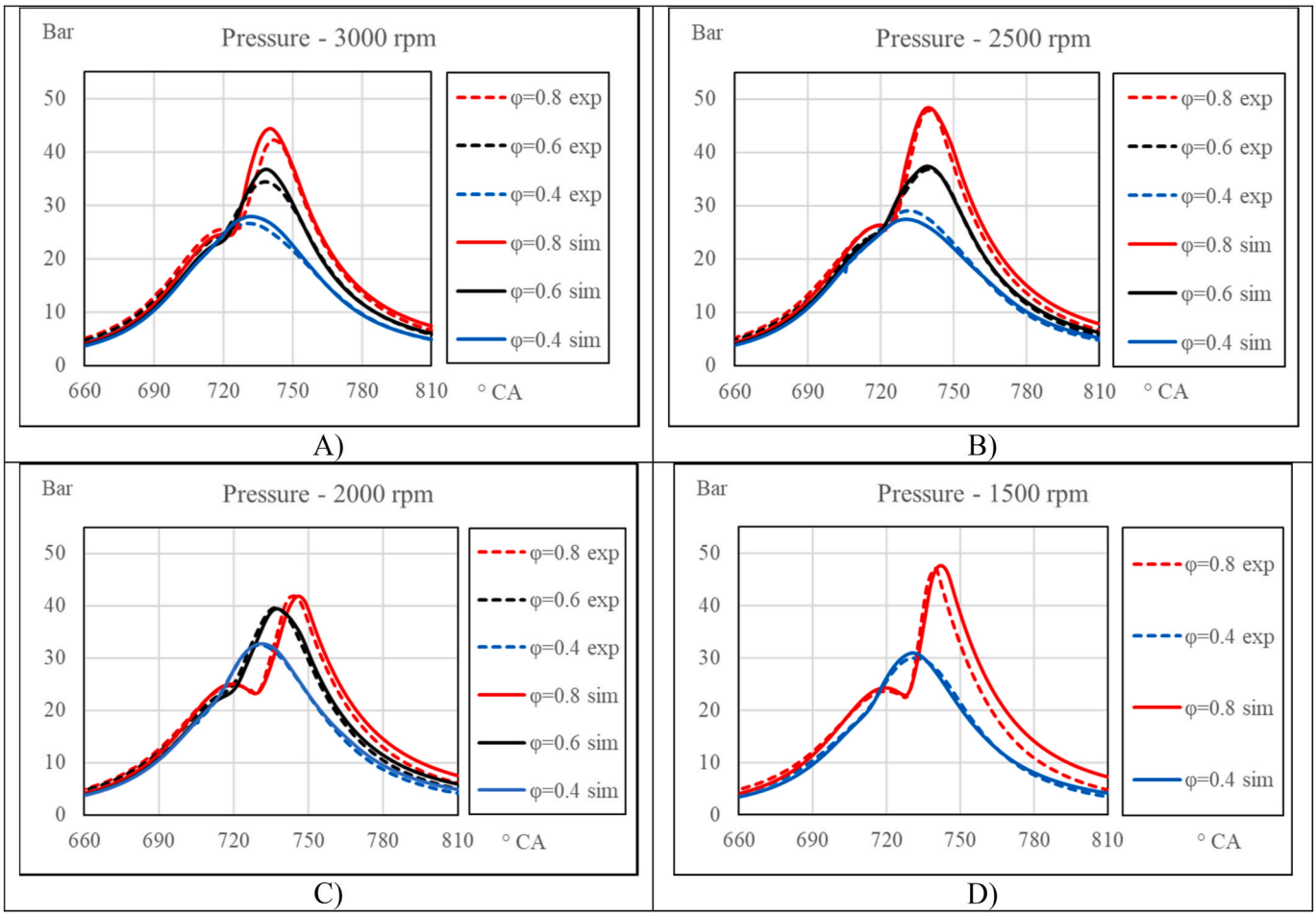

Fig. 26. Numerical-experimental comparison in terms of average in-cylinder pressure.

flow field is reported close to the TDC. The resulting intense flow field is able to deviate hydrogen jets, as shown in Fig. 16. H_2 is carried around the chamber and this limits a complete mixing with the air.

The consequence is a peculiar tendency of the investigated conditions to form regions of rich and lean mixture at the opposite sides of the combustion chamber, as visible in Fig. 17 which shows a comparison between the different equivalence ratios at 3000 rpm. In Fig. 18, the equivalence ratio probability density functions (PDFs) of the same cases show that the inhomogeneity increases with the average φ on equal revving speed and nearly equal injection start. This is motivated by the reduced mixing time for longer injection durations. The same comparison at 1500 rpm reveals an opposite trend. In fact, in Fig. 19, $\varphi = 0.8$ case is characterized by a more homogeneous mixture than the $\varphi = 0.4$ one. Such behavior is related to the short injection duration that characterizes $\varphi = 0.4$ cases. Since hydrogen is carried by the flow field around the chamber and the injection is short, fuel concentrates just in a limited sector of the cylinder. Increasing φ and thus the amount of fuel, the latter is more distributed along the circumferential direction, as shown in Fig. 20, promoting a more homogeneous mixture. This effect becomes more relevant at 1500 rpm than the one related to the reduction of time available for the mixing.

Considering the $\varphi = 0.8$ cases and comparing the equivalence ratio distribution for the different revving speeds as in Fig. 21, it is possible to notice that for lower rpm the mixture homogeneity improves, despite a lower turbulent kinetic energy as reported in Fig. 22. This emphasizes the dominant role of the mixing time over the turbulence intensity to achieve a uniform hydrogen-air mixture. At high revving speed (3000 rpm), the injection terminates close to the TDC, thus H_2 has no time to homogenize. At 1500 rpm, a greater time available for the mixing, leads to an extremely homogeneous mixture. Fig. 23 quantifies by means of PDFs the equivalence ratio distribution for all the engine speeds at $\varphi = 0.8$, confirming the presence of a more homogeneous mixture for lower engine speed.

The trend of the PDF with respect to the revving speed for $\varphi = 0.6$ is the same. As for $\varphi = 0.4$, instead, the fuel distribution homogeneity seems to be poorly sensitive to the rpm value, as visible in Fig. 24. Such behavior is due to the effect previously described and shown in Fig. 20, which is related to the short injection duration that characterizes $\varphi = 0.4$ cases. Because of the limited circumferential distribution of the fuel in the cylinder, the increasing available time for the mixing as the revving speed lowers cannot be adequately exploited.

Finally, an overview of the mixture homogeneity in all the cases is proposed by means of the standard deviation of hydrogen mass fraction, reported in Fig. 25.

As a conclusion of the cold flow analysis, it is possible to state that the proposed numerical framework is able to properly simulate flow field, injection process and mixing. Despite a direct validation is not possible, the capability of the model to reproduce the experiments will be confirmed in the following section on the combustion analysis of all the investigated conditions, whose numerical results are based on the presented injection and mixing analysis.

4.2.2. *Combustion*

Moving to the high-temperature cycle portion, numerical results are presented and compared to the experimental counterpart. As for the latter, data from test bench consist in phase-averaged pressure traces, and they are adopted as a reference for the model validation. An overall agreement is found between simulations and test bench measurements,

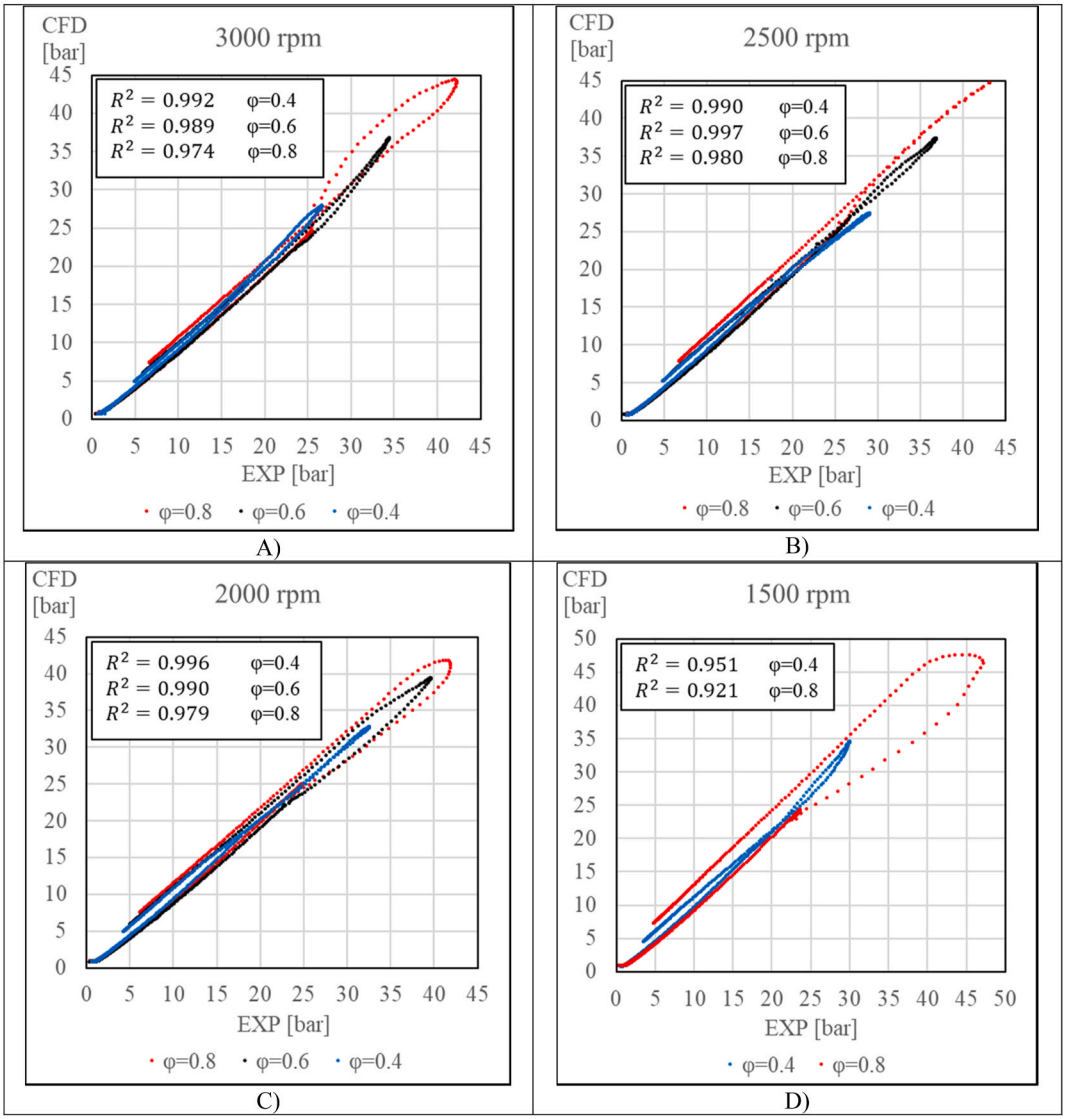

Fig. 27. Error analysis for all the calculated pressure traces.

as visible in Fig. 26. The major misalignment can be noticed for the case characterized by 1500 rpm and φ = 0.8, as the pressure is strongly underestimated during the expansion stroke. However, for this specific case, an inconsistency can be found in the experimental data. In fact, the in-cylinder pressure trace leads to an IMEP value that, combined with measured BMEP, results in an outlying FMEP value compared to the other cases.

An error analysis is carried out to quantify the differences between simulated and experimental pressure traces by means of the scatter plots reported in Fig. 27, in which the coefficient of determination R^2 is also reported. The latter is computed as in Eq. (14).

$$R^2 = 1 - \frac{\sum_{i=1}^{n} (y_i - \hat{y}_i)^2}{\sum_{i=1}^{n} (y_i - \bar{y})^2} \tag{14}$$

y_i and $\hat{y}_i$ are the experimental and computed pressure values for the crank angle i, respectively. $\bar{y}$ is the phase-average of the experimental pressure values. The computation is focused on the combustion interval 700°–810° CA.

The apparent heat release rate is analysed and reported in Fig. 28. The overall agreement between numerical and experimental outcomes is confirmed, and CFD is able to closely replicate phasing and duration of the investigated cases despite speed/mixture variation. Similarly to the comparison in terms of pressure, it is possible to individuate the misalignment during the expansion stroke for the case at 1500 rpm for φ = 0.8. In addition, it is evident that all the cases at 3000 rpm are affected by the same problem, that is combustion phasing is anticipated.

In order to highlight the capabilities of the numerical framework, Fig. 29 reports the mass fraction of burnt fuel (MFB) for a selection of cases. In particular, a sensitivity to the mixture quality on equal revving speed as well as the opposite are proposed in Fig. 29A) and B), respectively. In both the figures, only the extremal operating points are presented, for the sake of clarity. For a consistent comparison of the burn rates, the curves are shifted in the x-axis so that for each one the 50% of burnt mass occurs at 0° CA. This is motivated by the different start of combustion and MFB50% phasing of the original curves, hindering a clear comparison. In Fig. 29A) the numerical framework shows the correct sensitivity to the mixture quality. In Fig. 29B), instead, attention focuses on the revving speed. Despite a slight underestimation of the burn rate can be noticed at 1500 rpm, the sensitivity to the rpm value is coherent with the experiments, i.e. the combustion velocity nearly halves with the revving speed (as quantitatively confirmed in the following by the 10%–90% values), which means that it is almost constant considering the phenomenon on a time scale. The capability of the

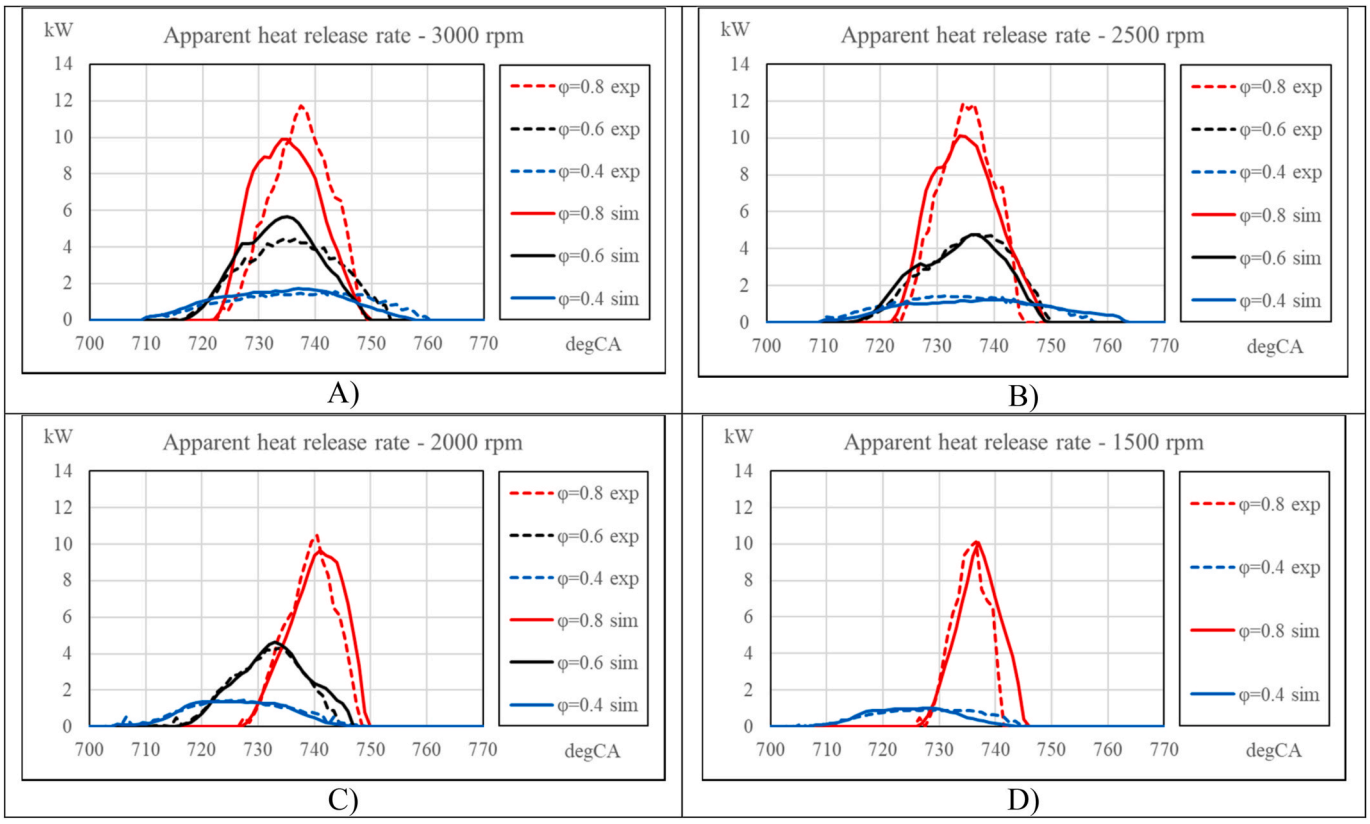

Fig. 28. Numerical-experimental comparison in terms of apparent heat release rate.

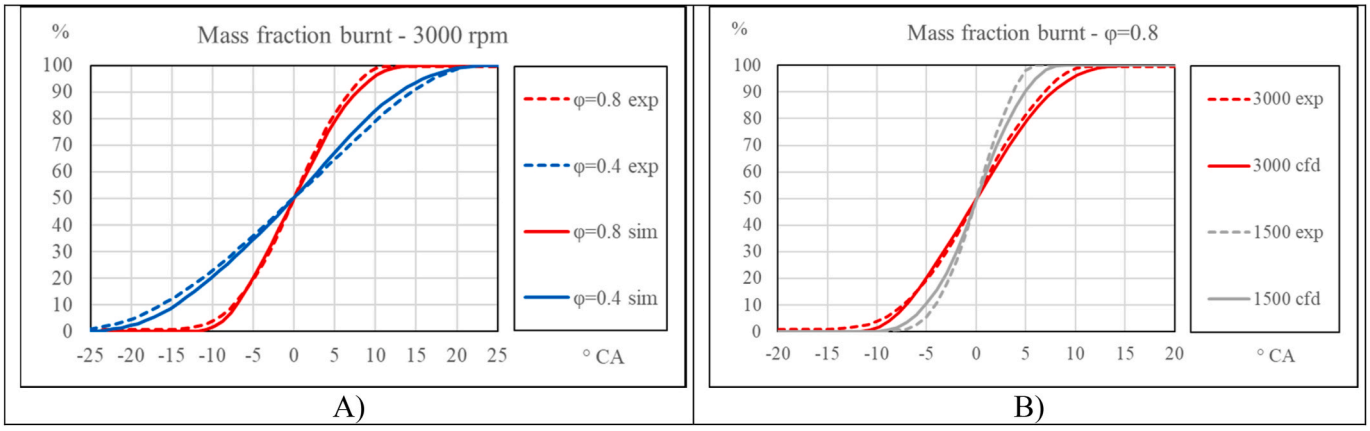

Fig. 29. A) mass fraction burnt at 3000 rpm and different mixture qualities; B) mass fraction burnt at φ = 0.8 and different revving speeds.

model to reproduce this behaviour is not trivial, considering the influences that simultaneously concur: on the one hand turbulence decreases with the rpm value, leading to a lower burn rate; on the other hand, the mixture is much more homogeneous at low revving speed, as confirmed by the PDF curves, leading to a higher combustion velocity.

In order to further quantify the agreement between CFD and experiments, Fig. 30 compares combustion phasing and duration for all the investigated cases. Starting from MFB50% (MFB50 in figure), operating conditions at 3000 rpm are characterized by a similar value and this is fairly reproduced by CFD. The same is valid at 2500 rpm as well, although CFD underestimates the MFB50% value for the φ = 0.4 case. At 2000 rpm and 1500 rpm experiments show a delayed combustion for increasing equivalence ratio and this is properly reproduced in the simulations. Moving to the duration, all the revving speeds are characterized by the same behaviour, that is 10%–90% duration reduces as the mean equivalence ratio increases, which is again well reproduced by the CFD simulations.

The characteristic swirl motion not only affects the mixing, but also the flame front propagation, as shown in Fig. 31. For brevity, only cases at 3000 rpm are proposed. A G = 0 iso-surface is visible at different CA and for different equivalence ratios, which should represent the position of the flame front. The latter is entrained by the flow field and rapidly consumes the mixture on the exhaust side. As shown in Fig. 17, for the φ = 0.4 case, the equivalence ratio on the exhaust side near the spark (bottom-right corner) is characterized by leaner values compared to the intake side. Therefore, the reason why the flame front propagates towards the exhaust for all the cases is not related to the mixture quality but, rather, to the effect of the local velocity field. Then, moving towards

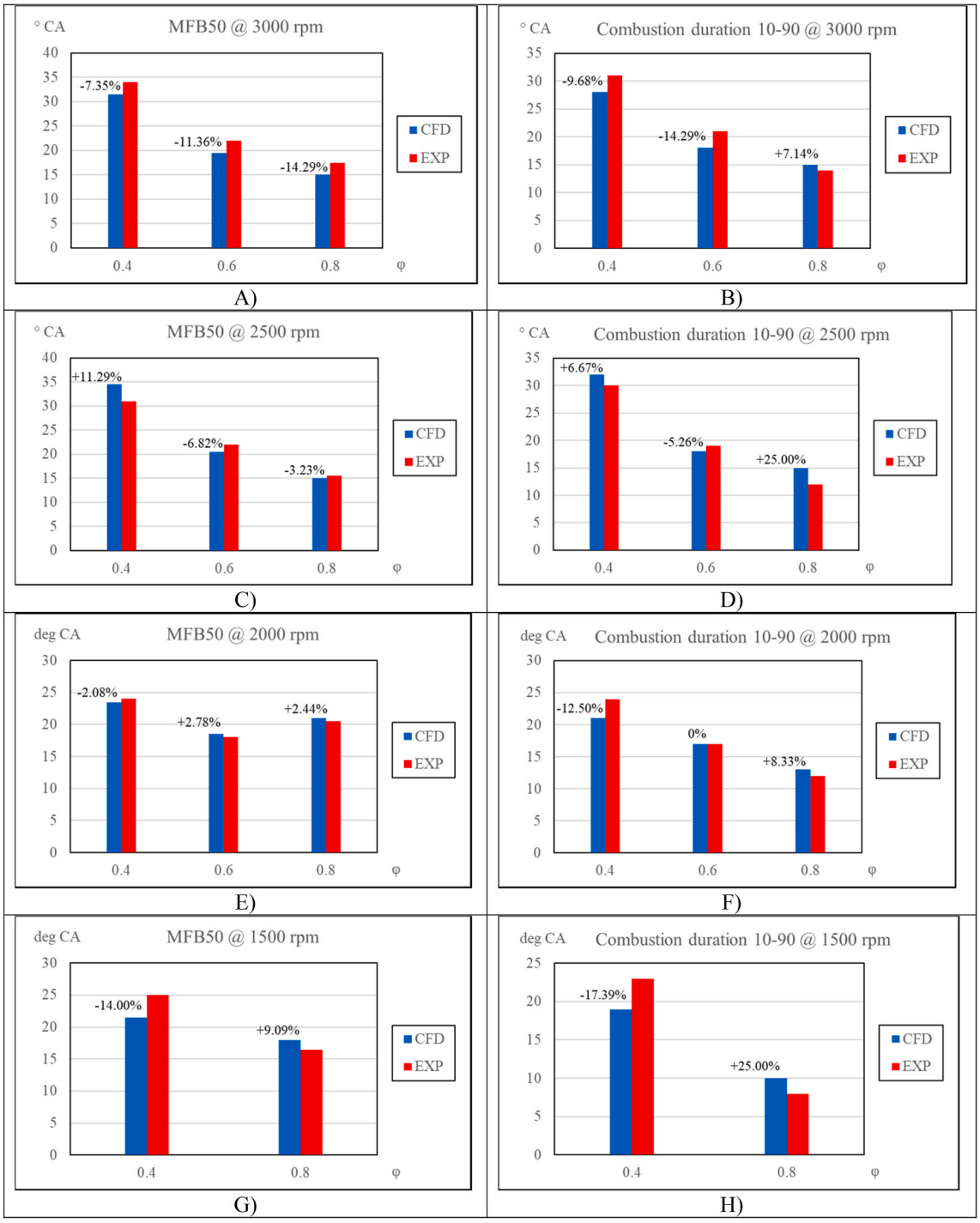

Fig. 30. Comparison in terms of combustion timing and duration for all the cases. A, C, E and G show the MFB50 at 3000 rpm, 2500 rpm, 2000 rpm and 1500 rpm, respectively; B, D, F and H report the combustion duration at 3000 rpm, 2500 rpm, 2000 rpm and 1500 rpm, respectively.

the end of the combustion process, the mixture on the intake side is consumed as well. It is interesting to notice that, despite the combustion start largely differs for the three cases (it occurs 4.5°, −3° and −12° CA BTDC), the end of the process is comparable. As visible at 720° CA, the flame front position strongly differs between the operating conditions, whereas at 740° CA it is comparable.

As a final remark on the results, it is possible to state that the capabilities of the proposed numerical framework are promising. A unique set-up (without case-by-case tuning) is adopted to simulate a considerable number of cases characterized by largely different mixture qualities and revving speeds. Moreover, very lean conditions are available among the investigated cases, which are of strong interest for the engine community working on H_2 ICEs. The agreement with respect to the experiments reveals that the proposed numerical framework constitutes a valuable tool to support the design of H_2 ICEs.

5. Conclusions

Work of researchers and designers in the ICE community is mainly oriented towards the reduction of the tailpipe emissions, especially CO_2 ones. Therefore, H_2 combustion is gaining more and more interest. 3D-CFD tools can be proficiently exploited to develop H2 ICEs and, for this

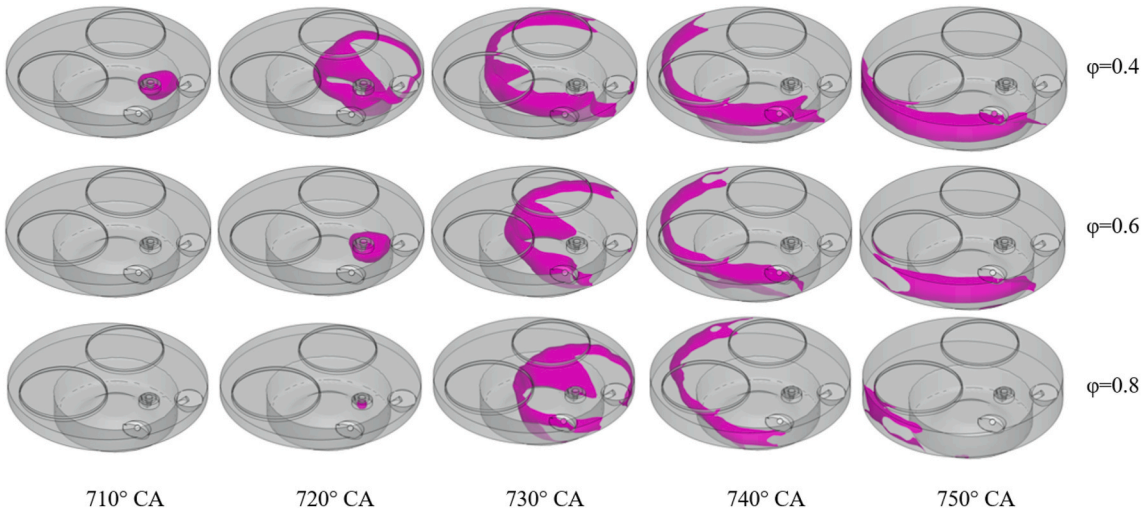

Fig. 31. Flame front propagation for the cases at 3000 rpm.

reason, a robust numerical methodology to simulate H_2 combustion in ICEs (even at very lean conditions, which are de facto the ones of main interest) is needed. The goal of the present work is to propose and extensively validate a numerical framework to be adopted in 3D-CFD combustion simulations of H_2 ICEs.

In the first part of the work attention is focused on the hydrogen injector. In particular, the possibility to simplify the geometry of the combustion chamber near the nozzles is investigated, in order to reduce the computational cost. Thanks to dedicated 3D-CFD vessel simulations, it is proven that the internal geometry of the injector can be neglected in the in-cylinder simulations without penalizing the quality of the results.

In the second part of the paper, 3D-CFD in-cylinder multi-cycle simulations are carried out at different conditions in terms of revving speed and equivalence ratio. Combustion is simulated even at very lean conditions ($\varphi = 0.4$) which are of outstanding interest for designers aiming at lowering NO_x emissions which represent the main drawback of the H_2 ICEs. Numerical results are validated against experimental measurements and an overall satisfying agreement is noticed without taking into account flame instability effects (even if for some operating points there is room for improvement). The most important outcome is that the agreement mentioned above is obtained with a unique setup of the numerical framework, that means no case-by-case tuning is carried out. This confirms the promising capabilities of the numerical framework which relies on in-house developed ignition and heat transfer models, a widely adopted flamelet combustion model, an improved correlation of laminar flame speed and a well-established turbulent flame speed correlation.

From a design point of view, simulations allow to point out the strong sensitivity to the time available for mixing and to the interaction between hydrogen jets and flow field.

In the near future, the present numerical approach will be improved to account for NO_x formation prediction thanks to a detailed chemistry approach and it will be validated against experimental measurements of NO_x emissions.

Declaration of competing interest

The authors declare that they have no known competing financial interests or personal relationships that could have appeared to influence the work reported in this paper.

Acknowledgments

The experimental work described in this paper has been conducted by Marco Antonelli and Luigi Martorano from the University of Pisa, in a regional project named 'H_2-Filiera idrogeno' promoted by Tuscany.

The authors gratefully acknowledge the University of Modena and Reggio Emilia for supporting the activity by the "Fondo di Ateneo per la Ricerca 2023 per il finanziamento di piani di sviluppo dipartimentale nell'ambito della ricerca" (FARD 2023).

Appendix A. Supplementary data

Supplementary data to this article can be found online at https://doi.org/10.1016/j.ijhydene.2023.12.027.

Symbols/abbreviations

A_k	Flame kernel surface
a_{inlet}	Sonic speed at inlet conditions
AHRR	Apparent Heat Release Rate
BC	Boundary Condition
BDC	Bottom Dead Center
BMEP	Brake Mean Effective Pressure
bTDC	before Top Dead Center
C	Progress variable
C_p	Specific heat at constant pressure
C_μ	Turbulent viscosity constant
CA	Crank Angle
CFD	Computational Fluid Dynamics
CFL	Courant-Friedrichs-Lewy
CI	Compression Ignition
CR	Compression Ratio
d_{gap}	Distance between spark electrodes
DI	Direct injection
ECFM	Extended Coherent Flamelet Model
FMEP	Friction Mean Effective Pressure
IMEP	Indicated Mean Effective Pressure
IVC	Intake Valve Closing
k	Thermal conductivity
$l_{F,t}$	Turbulent flame brush thickness
LES	Large Eddy Simulation
MFB	Mass Fraction Burnt
MIE	Minimum Ignition Energy
MON	Motor Octane Number
P	Pressure
PCC	Plume Combustion Concept
PDF	Probability Density Function

p_{inlet}	Inlet pressure
r_k	Flame kernel radius
RANS	Reynold Average Navier Stokes
RON	Research Octane Number
RPM	Revolution Per Minute
S	Throat section
S_L	Laminar flame speed
S_T	Turbulent flame speed
S_{plasma}	Expansion velocity of plasma channel
SI	Spark Ignition
SOI	Start Of Injection
ST	Spark Time
T	Temperature
T_k	Flame kernel temperature
TDC	Top Dead Center
TJI	Turbulent Jet Ignition
V	Volume
u'	Velocity fluctuations RMS
y^+	Dimensionless wall distance
Y	Mass fraction
δ_L	Laminar flame thickness
φ	Equivalence ratio
γ	Specific heats ratio
λ	Air-Fuel Equivalence Ratio ($1/\varphi$)
μ_l	Dynamic viscosity
ρ_{inlet}	Inlet density
ρ	Density
ρ_u	Unburnt density

References

[1] Reitz RD, et al. IJER editorial: the future of the internal combustion engine. Int J Engine Res Jan. 01, 2020;21(1):3–10. https://doi.org/10.1177/1468087419877990. SAGE Publications Ltd.

[2] Stępień Z. A comprehensive overview of hydrogen-fueled internal combustion engines: achievements and future challenges. Energies Oct. 01, 2021;14(20). https://doi.org/10.3390/en14206504. MDPI.

[3] Mazloomi K, Gomes C. Hydrogen as an energy carrier: prospects and challenges. Renew Sustain Energy Rev Jun. 2012;16(5):3024–33. https://doi.org/10.1016/j.rser.2012.02.028.

[4] Verhelst S, Wallner T. Hydrogen-fueled internal combustion engines. Prog Energy Combust Sci Dec. 2009;35(6):490–527. https://doi.org/10.1016/j.pecs.2009.08.001.

[5] Chand P, kumar Hod M. Hydrogen fueled I.C. Engine [Online]. Available: http://ijesc.org/; 2017.

[6] Verhelst S, Sierens R. Hydrogen engine-specific properties [Online]. Available: www.elsevier.com/locate/ijhydene; 2001.

[7] Boretti A. Stoichiometric H2ICEs with water injection. Int J Hydrogen Energy Apr. 2011;36(7):4469–73. https://doi.org/10.1016/j.ijhydene.2010.11.117.

[8] Mortimer J, Poursadegh F, Brear M, Yoannidis S, Lacey J, Yang Y. Extending the knock limits of hydrogen DI ICE using water injection. Fuel Mar. 2023;335:126652. https://doi.org/10.1016/j.fuel.2022.126652.

[9] Meng H, et al. Analyzing the effects of cooled EGR on the knock of hydrogen-fueled Wankel rotary engine. Int J Hydrogen Energy Sep. 2022;47(77):33094–104. https://doi.org/10.1016/j.ijhydene.2022.07.185.

[10] Xu H, Xiao B, Ni X, Luo Y, Zhang F, Weng C. The effect of the acoustically absorbing wall on the knocking phenomenon of hydrogen engines. Fuel Feb. 2023;333:126532. https://doi.org/10.1016/j.fuel.2022.126532.

[11] Karim GA. Hydrogen as a spark ignition engine fuel [Online]. Available: www.sciencedirect.comwww.elsevier.com/locate/ijhydene; 2003.

[12] Kalghatgi G, Head R, Chang J, Viollet Y, Babiker H, Amer A. An alternative method based on toluene/n-heptane surrogate fuels for rating the anti-knock quality of practical gasolines. Int J Franch Law 2014;7(3):663–72. https://doi.org/10.2307/26273706.

[13] Matalon M. The Darrieus-Landau instability of premixed flames. Fluid Dynam Res Aug. 2018;50(5). https://doi.org/10.1088/1873-7005/aab510.

[14] Onorati A, et al. The role of hydrogen for future internal combustion engines. Int J Engine Res Apr. 01, 2022;23(4):529–40. https://doi.org/10.1177/14680874221081947. SAGE Publications Ltd.

[15] Demuynck J, De Paepe M, Verhaert I, Verhelst S. Heat loss comparison between hydrogen, methane, gasoline and methanol in a spark-ignition internal combustion engine. Energy Proc 2012;29:138–46. https://doi.org/10.1016/j.egypro.2012.09.018.

[16] Shudo T. Improving thermal efficiency by reducing cooling losses in hydrogen combustion engines. Int J Hydrogen Energy Dec. 2007;32(17):4285–93. https://doi.org/10.1016/j.ijhydene.2007.06.002.

[17] Takagi Y, Oikawa M, Sato R, Kojiya Y, Mihara Y. Near-zero emissions with high thermal efficiency realized by optimizing jet plume location relative to combustion chamber wall, jet geometry and injection timing in a direct-injection hydrogen engine. Int J Hydrogen Energy Apr. 2019;44(18):9456–65. https://doi.org/10.1016/j.ijhydene.2019.02.058.

[18] Knop V, Benkenida A, Jay S, Colin O. Modelling of combustion and nitrogen oxide formation in hydrogen-fuelled internal combustion engines within a 3D CFD code. Int J Hydrogen Energy Oct. 2008;33(19):5083–97. https://doi.org/10.1016/j.ijhydene.2008.06.027.

[19] Gilmore EA, Lave LB, Adams PJ. The costs, air quality, and human health effects of meeting peak electricity demand with installed backup generators. Environ Sci Technol Nov. 2006;40(22):6887–93. https://doi.org/10.1021/es061151q.

[20] Heffel J. NOx emission reduction in a hydrogen fueled internal combustion engine at 3000 rpm using exhaust gas recirculation. Int J Hydrogen Energy Nov. 2003;28(11):1285–92. https://doi.org/10.1016/S0360-3199(02)00289-6.

[21] Younkins M, Wooldridge MS, Boyer BA. Port injection of water into a DI hydrogen engine. Apr. 2015. https://doi.org/10.4271/2015-01-0861.

[22] Yi HS, Lee SJ, Kim ES. Performance evaluation and emission characteristics of in-cylinder injection tipe fueled engine. 1996.

[23] Homan H, Deboer P, Mclean W. The effect of fuel injection on NOx emissions and undesirable combustion for hydrogen-fuelled piston engines. Int J Hydrogen Energy 1983;8(2):131–46. https://doi.org/10.1016/0360-3199(83)90095-2.

[24] Eichlseder H, Wallner T, Freymann R, Ringler J. The potential of hydrogen internal combustion engines in a future mobility scenario. Jun. 2003. https://doi.org/10.4271/2003-01-2267.

[25] Glasson N, Green R. Performance of a spark-ignition engine fuelled with hydrogen using a high-pressure injector. Int J Hydrogen Energy Nov. 1994;19(11):917–23. https://doi.org/10.1016/0360-3199(94)90046-9.

[26] White CM, Steeper RR, Lutz AE. The hydrogen-fueled internal combustion engine: a technical review. Int J Hydrogen Energy Aug. 2006;31(10):1292–305. https://doi.org/10.1016/j.ijhydene.2005.12.001.

[27] Jorach R. Development of a low-nox truck hydrogen engine with high specific power output*1. Int J Hydrogen Energy Apr. 1997;22(4):423–7. https://doi.org/10.1016/S0360-3199(96)00083-3.

[28] Green R, Glasson N. High-pressure hydrogen injection for internal combustion engines. Int J Hydrogen Energy Nov. 1992;17(11):895–901. https://doi.org/10.1016/0360-3199(92)90041-T.

[29] Varde K. Development of a high-pressure hydrogen injection for SI engine and results of engine behavior. Int J Hydrogen Energy 1985;10(11):743–8. https://doi.org/10.1016/0360-3199(85)90110-7.

[30] Stewart JR. CFD modelling of underexpanded hydrogen jets exiting rectangular shaped openings. Process Saf Environ Protect Jul. 2020;139:283–96. https://doi.org/10.1016/j.psep.2020.04.043.

[31] Guo P, Li X, Abu-Hamdeh NH, Bantan RAR. Mixing efficiency of hydrogen jet through multi lobe-injectors at scramjet engine: a numerical study. Aero Sci Technol Jan. 2022;120:107293. https://doi.org/10.1016/j.ast.2021.107293.

[32] Scarcelli R, Wallner T, Obermair H, Salazar VM, Kaiser SA. CFD and optical investigations of fluid dynamics and mixture formation in a DI-H2ICE. In: ASME 2010 internal combustion engine division fall technical conference. ASMEDC; Jan. 2010. p. 175–88. https://doi.org/10.1115/ICEF2010-35084.

[33] Barbato A, Cantore G. 3D CFD simulation of a gaseous fuel injection in a hydrogen-fueled internal combustion engine. E3S Web of Conferences Oct. 2021;312:07001. https://doi.org/10.1051/e3sconf/202131207001.

[34] Bhagat A, Gijare H, Dongari N. Numerical investigation of multi-species under-expanded SONIC jets. In: Proceeding of proceedings of the 24th national and 2nd international ISHMT-ASTFE heat and mass transfer conference (IHMTC-2017). Connecticut: Begellhouse; 2018. p. 987–92. https://doi.org/10.1615/IHMTC-2017.1370.

[35] Liu X, et al. Hydrogen pre-chamber combustion at lean-burn conditions on a heavy-duty diesel engine: a computational study. Fuel Mar. 2023;335:127042. https://doi.org/10.1016/j.fuel.2022.127042.

[36] Babayev R, Andersson A, Dalmau AS, Im HG, Johansson B. Computational characterization of hydrogen direct injection and nonpremixed combustion in a compression-ignition engine. Int J Hydrogen Energy May 2021;46(35):18678–96. https://doi.org/10.1016/j.ijhydene.2021.02.223.

[37] Maio G, et al. Experimental and numerical investigation of a direct injection spark ignition hydrogen engine for heavy-duty applications. Int J Hydrogen Energy Aug. 2022;47(67):29069–84. https://doi.org/10.1016/j.ijhydene.2022.06.184.

[38] Fontanesi S, Postrioti L, Magnani M, Martino M, Brizi G, Cicalese G. Preliminary assessment of hydrogen direct injection potentials and challenges through a joint experimental and numerical characterization of high-pressure gas jets. In: SAE technical papers. SAE International; Sep. 2022. https://doi.org/10.4271/2022-24-0014.

[39] Antonelli M, Martorano L. Realization and testing of a low pressure hydrogen direct injection engine using commercial injectors. In: SAE technical papers. SAE International; 2012. https://doi.org/10.4271/2012-01-0652.

[40] Antonelli M, Martorano L. Analisi numerica e sperimentale dei processi di iniezione e miscelamento in un piccolo motore ad iniezione diretta di idrogeno, vol. 67. Congresso Nazionale ATI – Trieste; 2012.

[41] Antonelli M, Martorano L. Analisi numerica E sperimentale dei processi di iniezione E miscelamento IN UN piccolo motore ad iniezione diretta di idrogeno. 2012.

[42] Simi A. Hydrogen direct injection in recirpocating engines using commercial injectors. PhD Dissertation; 2011.

[43] Scarselli M. Studio CFD dell'influenza della forma della camera di combustione di un motore ad iniezione diretta sul miscelamento tra aria ed idrogeno. Bachelor degree Thesis; 2013.
[44] Pavlovich Bulat Mikhail, Victorovich Bulat Pavel. Comparison of turbulence models in the calculation of supersonic separated flows. World Appl Sci J 2013;27 (10):1263–6.
[45] Yakhot V, Orszag SA. Renormalization group analysis of turbulence. I. Basic theory. J Sci Comput 1986;1(1):3–51. https://doi.org/10.1007/BF01061452.
[46] STAR-CD methodology guide.
[47] Teodosio L, Berni F. Optimization via genetic algorithm of a variable-valve-actuation spark-ignition engine based on the integration between 1D/3D simulation codes and optimizer. Int J Engine Res 2022. https://doi.org/10.1177/14680874221099874.
[48] Berni F, et al. A zonal secondary break-up model for 3D-CFD simulations of GDI sprays. Fuel Feb. 2022;309. https://doi.org/10.1016/j.fuel.2021.122064.
[49] Iacovano C, Berni F, Barbato A, Fontanesi S. A preliminary 1D-3D analysis of the darmstadt research engine under motored condition. In: E3S web of conferences. EDP Sciences; Oct. 2020. https://doi.org/10.1051/e3sconf/202019706006.
[50] Sparacino S, Berni F, Riccardi M, Cavicchi A, Postrioti L. 3D-CFD simulation of a GDI injector under standard and flashing conditions. In: E3S web of conferences. EDP Sciences; Oct. 2020. https://doi.org/10.1051/e3sconf/202019706002.
[51] Sparacino S, Berni F, D'Adamo A, Krastev VK, Cavicchi A, Postrioti L. Impact of the primary break-up strategy on the morphology of GDI sprays in 3D-CFD simulations of multi-hole injectors. Energies Jul. 2019;12(15). https://doi.org/10.3390/en12152890.
[52] Berni F, et al. Modeling of gaseous emissions and soot in 3D-CFD in-cylinder simulations of spark-ignition engines: a methodology to correlate numerical results and experimental data. Int J Engine Res 2022. https://doi.org/10.1177/14680874221112564.
[53] Berni F, Cicalese G, Borghi M, Fontanesi S. Towards grid-independent 3D-CFD wall-function-based heat transfer models for complex industrial flows with focus on in-cylinder simulations. Appl Therm Eng May 2021;190. https://doi.org/10.1016/j.applthermaleng.2021.116838.
[54] Berni F, Fontanesi S. A 3D-CFD methodology to investigate boundary layers and assess the applicability of wall functions in actual industrial problems: a focus on in-cylinder simulations. Appl Therm Eng Jun. 2020;174. https://doi.org/10.1016/j.applthermaleng.2020.115320.
[55] Berni F, Cicalese G, Sparacino S, Cantore G. On the existence of universal wall functions in in-cylinder simulations using a low-Reynolds RANS turbulence model. In: AIP conference proceedings. American Institute of Physics Inc.; Dec. 2019. https://doi.org/10.1063/1.5138752.
[56] Cicalese G, Berni F, Fontanesi S. Integrated in-cylinder/CHT methodology for the simulation of the engine thermal field: an application to high performance turbocharged DISI engines. SAE Int J Engines Apr. 2016;9(1):601–17. https://doi.org/10.4271/2016-01-0578.
[57] Berni F, Cicalese G, Fontanesi S. A modified thermal wall function for the estimation of gas-to-wall heat fluxes in CFD in-cylinder simulations of high performance spark-ignition engines. Appl Therm Eng 2017;115:1045–62. https://doi.org/10.1016/j.applthermaleng.2017.01.055.
[58] Cicalese G, Berni F, Fontanesi S, D'Adamo A, Andreoli E. A comprehensive CFD-CHT methodology for the characterization of a diesel engine: from the heat transfer prediction to the thermal field evaluation. In: SAE technical papers. SAE International; 2017. https://doi.org/10.4271/2017-01-2196.
[59] d'Adamo A, Iacovano C, Fontanesi S. Large-Eddy simulation of lean and ultra-lean combustion using advanced ignition modelling in a transparent combustion chamber engine. Appl Energy Dec. 2020;280. https://doi.org/10.1016/j.apenergy.2020.115949.
[60] D'Adamo A, Breda S, Cantore G. Large-eddy simulation of cycle-resolved knock in a turbocharged SI engine. In: Energy procedia. Elsevier Ltd; 2015. p. 45–50. https://doi.org/10.1016/j.egypro.2015.11.881.
[61] d'Adamo A, Breda S, Fontanesi S, Cantore G. LES modelling of spark-ignition cycle-to-cycle variability on a highly downsized DISI engine. SAE Int J Engines Sep. 2015;8(5):2029–41. https://doi.org/10.4271/2015-24-2403.
[62] Lee M, Hall M, Ezekoye O, Matthews R. Voltage, and energy deposition characteristics of spark ignition systems. SAE Technical Papers; Apr. 2005. https://doi.org/10.4271/2005-01-0231.
[63] Huang S, Li T, Ma P, Xie S, Zhang Z, Chen R. Quantitative evaluation of the breakdown process of spark discharge for spark-ignition engines. J Phys D Appl Phys 2020;53(4):045501. https://doi.org/10.1088/1361-6463/ab56da.
[64] Stevens CR. Energy storage and the criteria for proper ignition in the internal combustion engine. IEEE Trans Ind Electron Control Instrum 1965;IECI-12(1):8–13. https://doi.org/10.1109/TIECI.1965.229542.
[65] Tambasco C, Hall M, Matthews R. Spark discharge characteristics for varying spark plug geometries and gas compositions. 2022. https://doi.org/10.4271/2022-01-0437.
[66] Ravindra Arora WM. High voltage and electrical insulation engineering. second ed. 2022. 2nd Edition.
[67] Liao L, et al. A novel gas sensor based on field ionization from ZnO nanowires: moderate working voltage and high stability. Nanotechnology Apr. 2008;19:175501. https://doi.org/10.1088/0957-4484/19/17/175501.
[68] Meek JM, Craggs JD. Electrical breakdown of gases. A Wiley-Interscience publication. Wiley; 1978 [Online]. Available: https://books.google.it/books?id=1Xp5AAAAIAAJ.
[69] Ono R, Nifuku M, Fujiwara S, Horiguchi S, Oda T. Minimum ignition energy of hydrogen–air mixture: effects of humidity and spark duration. J Electrost Feb. 2007;65(2):87–93. https://doi.org/10.1016/j.elstat.2006.07.004.
[70] Herweg R, Maly RR. A fundamental model for flame kernel formation in S. I. Engines. SAE Trans 1992;101:1947–76 [Online]. Available: http://www.jstor.org/stable/44611342.
[71] Colin O, Truffin K. A spark ignition model for large eddy simulation based on an FSD transport equation (ISSIM-LES). Proc Combust Inst 2011;33(2):3097–104. https://doi.org/10.1016/j.proci.2010.07.023.
[72] Siemens PLM. DARS v2020.1 manual - book 2. 2020.
[73] Shrestha KP, Seidel L, Zeuch T, Mauss F. Detailed kinetic mechanism for the oxidation of ammonia including the formation and reduction of nitrogen oxides. Energy Fuels Oct. 2018;32(10):10202–17. https://doi.org/10.1021/acs.energyfuels.8b01056.
[74] Siemens PLM. STARCD v4.34 manual - methodology. 2020.
[75] Bruneaux G. Asymptotic analysis, direct numerical simulation and modeling of premixed turbulent flame-wall interaction; Etude asymptotique, simulation numerique directe et modelisation de l'interaction flamme turbulente premelangee-paroi. Ph.D. Thesis. Institut Francais du Petrole (IFP), 92 - Rueil-Malmaison (France); 1996.
[76] Verhelst S, Tjoen C, Vancoillie J, Demuynck J. A correlation for the laminar burning velocity for use in hydrogen spark ignition engine simulation. Int J Hydrogen Energy Jan. 2011;36(1):957–74. https://doi.org/10.1016/j.ijhydene.2010.10.020.
[77] Konnov AA. Refinement of the kinetic mechanism of hydrogen combustion. Adv Chem Phys 2004;23:5–18.